European Journal of Inorganic Chemistry

EurJIC
European Journal of Inorganic Chemistry

Chemistry Europe
European Chemical Societies Publishing

RESEARCH ARTICLE OPEN ACCESS

Tetra-Cationic Pyridyl-Porphyrins With Peripheral Rhenium(I) Complexes: Photophysics, Photobiological, and BSA-Binding Properties

Rafaela C. Copello[1] | André S. Polo[2] | Rafael de Q. Garcia[3] | Leonardo De Boni[3] | Luiz Antônio Sodré Costa[4] | Henrique F. V. Victória[5] | Klaus Krambrock[5] | Otávio A. Chaves[6,7] | Bernardo A. Iglesias[1]

[1]Laboratório de Bioinorgânica e Materiais Porfirínicos, Departamento de Química, Universidade Federal de Santa Maria - UFSM, Santa Maria, Brazil | [2]Centro de Ciências Naturais e Humanas, Universidade Federal do ABC - UFABC, Santo André, Brazil | [3]Instituto de Física de São Carlos, Universidade de São Paulo – USP-SC, São Carlos, Brazil | [4]NEQC – Núcleo de Estudos em Química Computacional, Departamento de Química, ICE, Universidade Federal de Juiz de Fora - UFJF, Juiz de Fora, Brazil | [5]Departamento de Física, Universidade Federal de Minas Gerais - UFMG, Belo Horizonte, Brazil | [6]Departamento de Química, Centro de Química de Coimbra - Instituto de Ciências Moleculares, Universidade de Coimbra - UC, Coimbra, Portugal | [7]Laboratório de Imunofarmacologia, Centro de Pesquisa, Inovação e Vigilância em COVID-19 e Emergências Sanitárias (CPIV), Instituto Oswaldo Cruz Institute, Fundação Oswaldo Cruz - FIOCRUZ, Rio de Janeiro, Brazil

Correspondence: Bernardo A. Iglesias (bernardopgq@gmail.com; bernardo.iglesias@ufsm.br)

Received: 10 October 2025 | **Revised:** 11 November 2025 | **Accepted:** 18 November 2025

Keywords: bovine serum albumin | photobiology | photophysics | porphyrins | rhenium(I) complexes

ABSTRACT

In this article, isomeric tetra-cationic porphyrins with rhenium(I)-carbonyl-phenanthroline complexes at the peripheral N-pyridyl positions **3ReP** and **4ReP** were evaluated for structural characterization, photophysical properties, theoretical calculations, electrochemical behavior, and photobiological properties. Furthermore, photostability, reactive oxygen species generation, and binding properties on bovine serum albumin protein were assessed using absorption, steady-state, and time-resolved fluorescence emission, with molecular docking analysis.

1 | Introduction

Porphyrins are a highly significant class of 18 π-electron conjugated molecules, exhibiting biological, catalytic/electrocatalytic, photochemical, and photophysical properties. Due to their extensive applications as hybrid nano- or biomaterials, this class of macrocycles displays several properties explored in various fields, such as supramolecular chemistry, catalysis, medicinal applications, materials chemistry, and bioinorganic science [1–4].

Rhenium(I) polypyridyl compounds have garnered substantial attention due to their photochemical and photophysical properties, primarily associated with their lowest-lying triplet metal-to-ligand charge transfer (^{3}MLCT) excited state [5]. The energy of this excited state is often sufficient for several processes, such as intramolecular isomerization, which can be modulated by altering the ^{3}MLCT energy through substituent modification in polypyridyl ligands with electron acceptor or donor groups [6]. This modification has potential applications in molecular switches, for example. This process is also dependent on the substituent of the isomerizable moiety [7]. The characteristics of these compounds are also crucial for solar energy conversion. In this context, rhenium(I) compounds have been employed in the photo-assisted reduction of carbon dioxide (CO_2) to other compounds, thereby storing sunlight in chemical form [8, 9, 10]. The use of appropriate polypyridyl ligands can enhance efficiency in these systems [11], and changing the sacrificial electron donor can also modulate conversion performance [12].

Several examples of porphyrin derivatives containing peripheral Re(I) complexes are documented in the literature, reported by research groups such as those of Indelli and Iengo [13, 14], Perutz [15, 16, 17], Alessio [18, 19, 20], and Satake

[21, 22, 23, 24, 25] among others. According to the reported data, studies have focused on photocatalytic CO_2 reduction, electron/energy transfer phenomena, and interaction with DNA. It is observed that using peripheral modifications in the porphyrins is possible to increase the thermodynamic stability of the supramolecular adducts at room temperature [14], as well as increase the water solubility of the porphyrins, which is very interesting for clinical application, considering the administration and efficacy [20].

In this article, isomeric tetra-cationic porphyrins with rhenium(I)-carbonyl-phenanthroline complexes at the peripheral positions **3ReP** and **4ReP** (Figure 1) were evaluated for structural characterization, photophysical properties, time-dependent density functional theory calculations, electrochemical properties, and photobiological properties. Furthermore, photostability, reactive oxygen species (ROS) generation, and binding properties on bovine serum albumin (BSA) protein were assessed using absorption, steady-state, and time-resolved fluorescence emission, and molecular docking calculations.

2 | Experimental Section

All reagents used were of analytical grade and purchased from Sigma–Aldrich, Start Bioscience, or national suppliers, without preliminary purification. The BSA protein was lyophilized powder and fatty acid-free (Sigma–Aldrich; purity ≥ 99%). The concentration of the BSA stock solutions was confirmed by UV–Vis

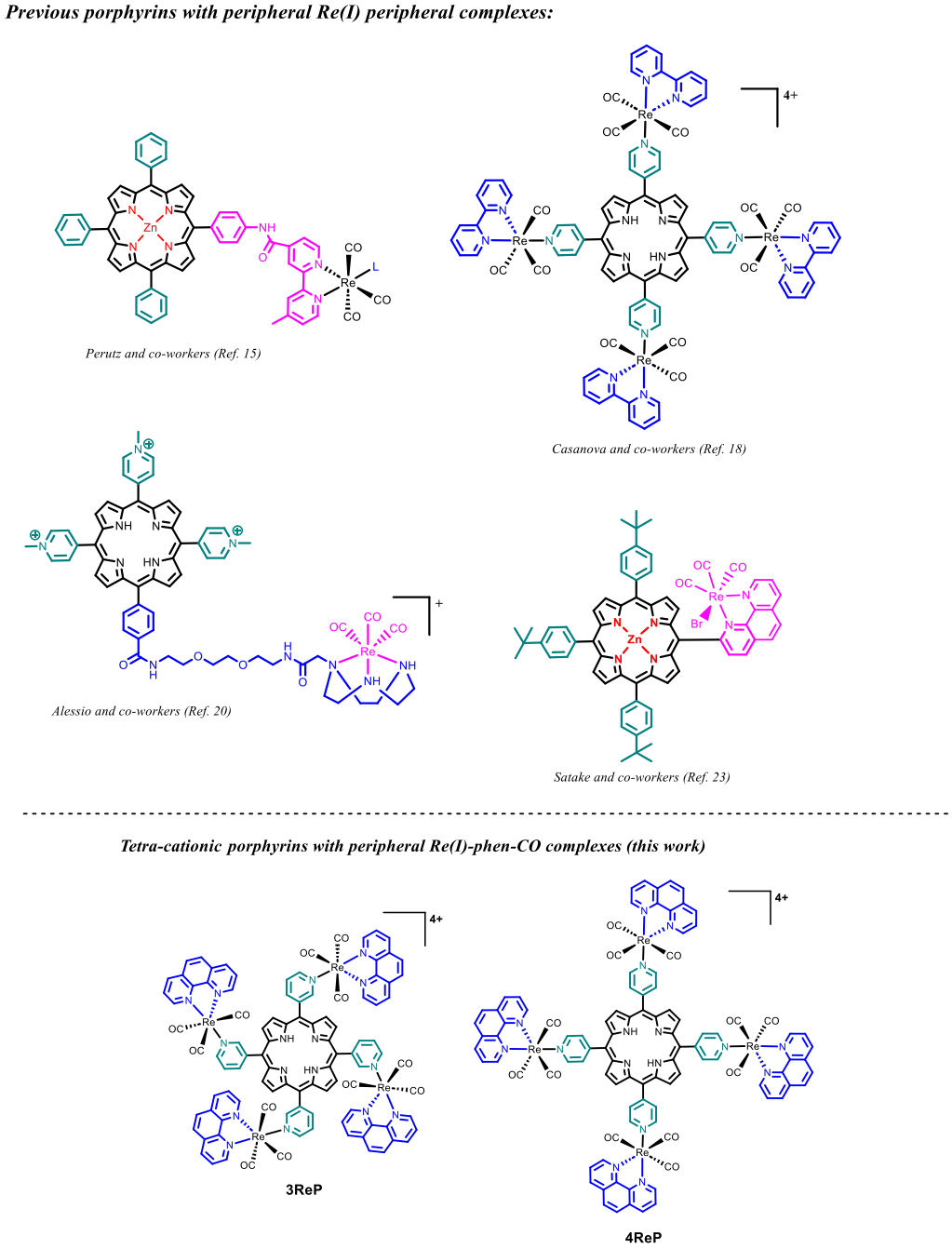

FIGURE 1 | Overview of porphyrins with peripheral Re(I) complexes. All counterions are omitted for clarity.

analysis using the Beer–Lambert equation, with the molar absorptivity (ε) value of 43,825 M^{-1} cm^{-1} at 280 nm in a Tris-HCl pH 7.4 buffer solution. The water used in all experiments was of Milli-Q grade.

2.1 | General Characterization

Porphyrins **3ReP** and **4ReP** were analyzed using a high-resolution mass spectrometer with electrospray ionization (HRMS-ESI) in the positive mode with a micrOTOF-QII mass spectrometer (Bruker Daltonics, USA). Mass spectra were recorded for each sample in methanolic solution (500 ppb) with a flow of 180 μL min^{-1} and capillarity of 6000 V. Elemental analyses (CHN%) were performed using a Shimadzu EA112 microanalysis instrument. The molar conductance of the porphyrins in a 10^{-4} M DMF solution at 298K was measured using an MS Tecnopon model mCA 150.1 direct-reading conductivity bridge, calibrated with 0.01 M KCl in duplicate. The ^{1}H nuclear magnetic ressonance (NMR spectra were recorded on a Bruker Avance III spectrometer at 600 MHz, respectively. DMSO-$_{d6}$ was used as the solvent and tetra(methyl)silane (TMS) as the internal reference. The Fourier-transform infrared (FTIR) spectra in transmission mode were recorded on a Bruker Vertex 70 spectrometer with an ATR accessory in the 4000–400 cm^{-1} region with 64 scans and 4 cm^{-1} resolution.

2.2 | Luminescence

Absorption and fluorescence spectra were determined using a Shimadzu UV-1800 spectrophotometer and a Hitachi F7000 fluorimeter, respectively. Absorption measurements were conducted from 200 to 1100 nm for all porphyrins dissolved in acetonitrile (MeCN) or *N*,*N*′-dimethylformamide (DMF). The porphyrin samples were contained in a 1.0 mm optical path length fuzed silica cuvette with concentrations of ≈10 μM.

For fluorescence spectra monitored in the 600–800 nm range, samples were held in a 1.0 cm fuzed silica cuvette at a concentration of ≈1.0 μM to prevent fluorescence reabsorption. The fluorescence quantum yields (Φ_f) of the porphyrins dissolved in MeCN or DMF were measured using Brouwer's method and the same fluorimeter [26, 27]. Hematoporphyrin IX was used as a reference for Brouwer's method, with a well-known Φ_f of about 8.0% in DMSO. The fluorescence quantum yields were determined after recording the steady-state fluorescence spectra for all porphyrin samples.

Time-resolved fluorescence techniques using femtosecond laser pulses [26] were employed to determine the fluorescence lifetime (τ_f). Samples were excited at the Soret and Q-bands, and the fluorescence signal was monitored using a Si-photodetector coupled to a 1.0 GHz digital oscilloscope.

The intersystem crossing rate (k_{isc}) and triplet state quantum yield formation (Φ_T) were determined using two consecutive laser pulses at 515 nm that excited the porphyrins in the same spatial region with a time interval of about 15 ns between pulses. This double excitation yielded two fluorescence decay curves. By analyzing the fluorescence quenching as a function of the pulse energies, which reflects the population transition to the long-lifetime triplet state, the mechanism of triplet population formation was evaluated. More details about this technique can be found elsewhere [26, 27].

2.3 | Theoretical Calculation

Metallic complexes **3ReP** and **4ReP** were studied using density functional calculations (DFT) calculations to obtain minimum-energy optimized geometries and electronic properties. Both complexes were optimized with the GFN2-xTB Hamiltonian, including an implicit solvation effect via the DDCOSMO polarizable continuum model with acetonitrile as solvent [28, 29, 30]. Global Optimizer Algorithm was used to confirm the global minimum structures [31]. To analyze the frontier molecular orbitals and gain insight into the nature of the electronic transitions, simplified Tamm–Dancoff (sTDA) density functional calculations were carried out using the range-separated hybrid functional CAM-B3LYP with Ahlrich's def2-SVP basis set, considering 30 excitations (all excitations up to 5.0 eV were taken into consideration) [32, 33, 34]; DDCOSMO solvation model was also employed in these calculations. All computations were performed with the ORCA quantum chemistry package [35] on Dell servers at the NEQC-UFJF facilities.

2.4 | Electrochemistry and Spectroelectrochemistry Analysis

Cyclic voltammograms were recorded in MeCN solutions (electrochemical grade; Sigma–Aldrich) using an EcoChemie AutoLab PGSTAT 128N system at room temperature under an argon atmosphere. Electrochemical grade tetrabutylammonium hexafluorophosphate ($TBAPF_6$, Sigma–Aldrich) was used as the supporting electrolyte (0.1 M). These cyclic voltammetry (CV) experiments were performed using a standard three-component system: a glassy carbon working electrode, a platinum wire auxiliary electrode, and a platinum wire *pseudo*-reference electrode. Ferrocene/ferrocenium was used as an internal reference and converted to normal hydrogen electrode (NHE) [36]. Spectroelectrochemistry data were collected using a previously described homemade thin-layer cell [37], a portable PalmSens EmStat4S potentiostat/galvanostat, and the Shimadzu UV1600 spectrophotometer.

2.5 | Aggregation and Solution Stability Study by Absorption Analysis

To investigate the possible aggregation of the studied porphyrins **3ReP** and **4ReP**, UV–Vis spectra were measured as a function of concentration using DMF and DMF (5%)/Tris-HCl pH 7.4 buffer solutions. The λ_{Soret} change in the transition band in the UV–Vis spectrum was monitored. Solution stability studies of porphyrins in the same solutions were conducted by absorption analysis over a period of 7 days.

2.6 | Water/n-Octanol Partition Coefficients (Log P_{OW})

The log P_{OW} value was calculated and recorded according to the literature [38], using the maximum absorbance of the Soret band and volumes in the organic and aqueous phases, respectively.

2.7 | Photobiological Properties

2.7.1 | ROS Generation by Electron Paramagnetic Resonance (EPR)

The EPR experiments combined with the spin trapping methodology were performed on a commercial MiniScope MS400 spectrometer (Magnettech, Germany) operating in the X-band (microwave frequency ≈9.4 GHz). The experimental parameters used were: 10 mW microwave power, 100 kHz modulation field with an amplitude of 0.2 mT, center field of 337 mT, sweep range of 10 mT, scan time of 60 s, and 4096 integration points. All EPR spectra were measured at room temperature. The spin traps used in this experiment were N-tert-butyl-α-phenylnitrone (PBN, 99%; Tokyo Chemical Industry Company, Japan) and 5,5-dimethyl-1-pyrroline N-oxide (DMPO, 96%; Oakwood Chemicals, USA). The redox probe used for singlet oxygen ($^1O_2$) quantification was Hydroxy-TEMP (2,2,6,6-tetramethylpiperidinol, 99%, Sigma–Aldrich).

Initially, stock solutions of MeCN were prepared in conical tubes containing powdered samples (205 μM). Using the molecular weights of the porphyrins, the concentrations of the stock solutions were calculated based on the predicted mass values. Samples were diluted to a final concentration of 100 μM. Aliquots for EPR spectra were prepared using ¼ of the total volume containing an acetonitrile solution with the porphyrin at 100 μM, ½ of the total volume containing an acetonitrile solution with the spin trap/redox probe, and ¼ of the volume completed with acetonitrile. The solutions were then illuminated with a white LED lamp (irradiance of 12 mW cm^{-2}), and aliquots were collected at different predefined time intervals, filled into glass capillaries (50 μL), and placed into a quartz tube for EPR measurement.

2.7.2 | Photostability Assays, Singlet Oxygen Generation, and Superoxide Parameters

Photostability experiments of porphyrins **3ReP** and **4ReP** in DMF and DMF(5%)/Tris-HCl pH 7.4 buffer solutions were monitored by UV–Vis absorption measurements at different exposure times (0 to 10 min) under a white-light LED array system (400 to 800 nm) at an irradiance of 25 mW cm^{-2} and a total light dosage of 30 J cm^{-2}. All experiments were performed in duplicate and independently.

Singlet oxygen photodegradation experiments were performed using the quencher 1,3-diphenylisobenzofuran (DPBF), containing 100 μM DPBF in DMF or MeCN, mixed with each porphyrin (10 μM). To measure $^1O_2$ generation, UV–Vis spectra were recorded for each solution (sample and standard) at different exposure times using a white-light LED array system (400 to 800 nm) at an irradiance of 25 mW cm^{-2} and a total light dosage of 30 J cm^{-2} at a distance of 5.0 cm from the cuvette sample. The $^1O_2$ quantum yield (Φ_Δ) was calculated according to the literature [39, 40, 41] with *meso*-tetra(phenyl)porphyrin (TPP) dissolved in DMSO ($\Phi_\Delta = 0.52$) as the standard molecule [42].

Superoxide radical ($O_2^{\bullet-}$) species were assessed by nitro blue tetrazolium (NBT) reduction assays conducted under conditions cited in the literature, using NBT and NADH in a DMF solution [43]. Control experiments were conducted without porphyrins, and derivatives were irradiated under aerobic conditions with a white-light LED source (irradiance of 25 mW cm^{-2} and a total light dosage of 30 J cm^{-2}) for 10 min. The reaction progress was monitored by the increase in absorbance near $\lambda = 560$ nm. The superoxide generation constant (k_{SO}) values were obtained as per the aforementioned literature [44].

2.8 | Biomacromolecule Binding Studies

2.8.1 | BSA-Binding Assays by Steady-State Fluorescence Emission Analysis

Binding parameters between BSA and related porphyrin derivatives, **3ReP** and **4ReP** ([porphyrins] = 0–20 μM), were obtained by emission measurements at four temperatures (298, 303, 308, and 315 K) in a DMF(5%)/Tris-HCl pH 7.4 buffer solution in the 300–500 nm range (BSA = 5.0 μM), using an excitation source at 295 nm. The data from the fluorescence quenching and binding experiments were analyzed using the Stern–Volmer (K_{SV}), modified Stern–Volmer (K_a), the number of fluorophores (f), and Gibb's free energy ($\Delta G°$) parameters, according to literature equations [45]. An analysis of the thermodynamic parameters of the interaction with BSA was determined through the van't Hoff equation, by the values of enthalpy ($\Delta H°$) and entropy ($\Delta S°$) at the aforementioned temperatures [37]. In addition, the inner filter correction was applied to the steady-state fluorescence data [46].

2.8.2 | Synchronized Fluorescence (SF) Emission and Site Marker Assays

The SF spectra of porphyrins **3ReP** and **4ReP** were recorded for BSA (5.0 μM) both in the absence and presence of each porphyrin (concentration ranging from 0 to 200 μM) at 298 K. Spectra were recorded in the 240–320 nm range by setting $\Delta\lambda = 15$ nm (for tyrosine residues) and $\Delta\lambda = 60$ nm (for tryptophan residues), respectively. Competitive binding studies with porphyrins into site III of BSA were performed in the presence of the site marker, digitoxin (DGX), which was selected through molecular docking calculations. Both BSA and the site marker were maintained at a 1:1 concentration ratio. Before adding the porphyrins to the albumin solution, BSA and the site marker were incubated for 5 min at 298 K. Subsequent Re(I)-porphyrin additions were conducted at the same concentrations as in the steady-state fluorescence description above.

2.8.3 | Time-Resolved Fluorescence Decay with BSA

Fluorescence lifetime decays (τ_f) were recorded using the time-correlated single photon counting method with a DeltaHub controller in conjunction with a Horiba Jobin-Yvon Fluoromax Plus spectrofluorometer. A NanoLED (Horiba) source (1.0 MHz, pulse width < 1.2 ns at 284 nm excitation wavelength) was used as an excitation source. The concentrations of BSA (5.0 μM) and porphyrins (20 μM) were fixed, each in a DMF(5%)/Tris-HCl pH 7.4 buffer solution.

2.8.4 | Molecular Docking Calculation Analysis

The crystallographic structure for nonbound BSA was obtained from the Protein Data Bank (access code 4F5S) [47]. The chemical structures of **3ReP** and **4ReP** were built and energy-minimized using a semiempirical method with Spartan18 software (Wavefunction, Inc., Irvine, CA, USA). The molecular

docking calculations were performed with GOLD 2023.3 software (Cambridge Crystallographic Data Centre, Cambridge, CB2 1EZ, UK). Hydrogen atoms were added to the protein, considering a pH of 7.4. A 12 Å radius around each of the three subdomains of the BSA structure (subdomains IIA, IIIA, and IB) [48, 49] was defined for in silico calculations, and ChemPLP was used as the scoring function due to its best correlation between experimental and in silico data previously reported for porphyrins and albumin [50, 51, 52]. The Protein–Ligand Interaction Profiler was used to identify the main amino acid residues, and the three-dimensional figures were generated with PyMOL Molecular Graphics System 1.0-level software (Delano Scientific LLC software, Schrodinger, New York, USA).

3 | Results and Discussion

3.1 | Synthesis of Derivatives 3ReP and 4ReP

Rhenium(I) precursor complex and the corresponding isomeric tetra-cationic porphyrins were synthesized as described in the literature, with some modifications [7, 19]. In this synthetic route, *meso*-tetra(pyridyl)porphyrins (1.0 equivalent) react in a chloroform solution at 50°C with a slight excess of *fac*-[Re(phen)$(CO)_3$(OTf)] (4.05 equivalents) for 8 h, followed by precipitation with hexane and recrystallization in acetone (Scheme 1). These Re(I)-porphyrins, **3ReP** and **4ReP,** were also synthesized, and all compounds were analyzed by CHN%, HRMS-ESI, and molar conductometry analysis. Additionally, synthetic details, microanalysis, NMR, and FTIR data are provided in Supporting Information section (Table S1 and Figures S1–S6).

3.2 | Photophysical Properties of the Porphyrin Derivatives

Figure 2 shows the molar extinction coefficient, ε, and normalized fluorescence are illustrated for all porphyrins dissolved in MeCN or DMF solutions, respectively. The Soret band absorption is observed in the 414–419 nm range for all derivatives with values between 1.10 and 2.0×10^5 M^{-1} cm^{-1} (Table 1). The Q-bands are located between 500 and 650 nm, showing no significant

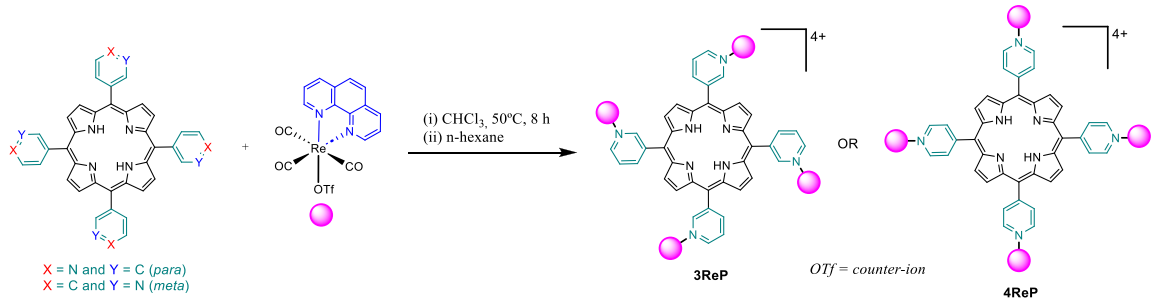

SCHEME 1 | Synthetic route of porphyrins **3ReP** and **4ReP**.

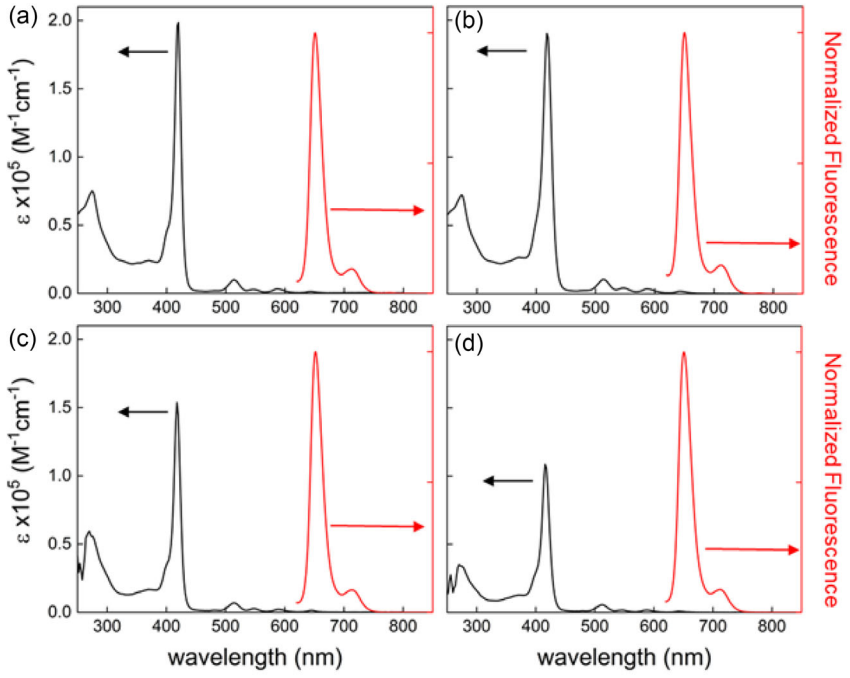

FIGURE 2 | Molar excitation coefficients (black lines) and steady-state fluorescence (red lines) spectra of the porphyrins **3ReP** and **4ReP** dissolved in (a,b) MeCN and (c,d) DMF, respectively.

TABLE 1 | Photophysical properties of the Re(I)-porphyrins derivatives **3ReP** and **4ReP**.

MeCN								
Porphyrin	λ_{Soret} (nm)	λ_{Emiss} (nm)	ϕ_f (%)	τ_f (ns)	k_r (10^6 s^{-1})	k_{ic} (10^8 s^{-1})	k_{isc} (10^8 s^{-1})	ϕ_T (%)
3ReP	419	651,710	1.8 ± 0.2	3.0 ± 0.1	6.7	1.7	1.6	48 ± 2
4ReP	418	652,712	3.6 ± 0.3	4.2 ± 0.2	7.9	1.3	1.0	43 ± 2
DMF								
Porphyrin	λ_{Soret} (nm)	λ_{Emiss} (nm)	ϕ_f (%)	τ_f (ns)	k_r (10^6 s^{-1})	k_{ic} (10^8 s^{-1})	k_{isc} (10^8 s^{-1})	ϕ_T (%)
3ReP	418	652,711	2.9 ± 0.2	3.2 ± 0.1	8.4	1.3	1.7	46 ± 2
4ReP	416	652,710	4.1 ± 0.3	4.3 ± 0.2	8.6	1.3	0.9	37 ± 2

wavelength shift when comparing porphyrins and the selected solvents. The absorption band at 280–300 nm is associated with the phenanthroline (phen) intraligand transition band (IL).

Regarding the fluorescence spectra, the maximum emission occurs at ≈651 nm for all derivatives in both solvents. Essentially, the quantity of Re(I)-porphyrins and the transition between MeCN and DMF solvents do not significantly affect the wavelength position and line shape of the porphyrins, considering the experimental error of ≈1.0 nm. This can be attributed to the negligible difference in dielectric constants between the two solvents, with MeCN being slightly higher.

The fluorescence quantum yield (ϕ_f) values were obtained for all derivatives in both solvents using Brouwer's method, as previously mentioned, and are depicted in Table 1. When comparing each porphyrin in both solvents, it is noted that the ϕ_f is slightly lower in MeCN solution. This observation can also be explained by the solvent's dielectric constant. Among porphyrins with identical side charge groups at the *meta* (**3**) and *para* (**4**) positions, the ϕ_f is higher for those with groups in the *para* position. The value increases by at least 35% for **4ReP** compared to **3ReP** in DMF (Table 1). For **4ReP** dissolved in MeCN, the ϕ_f increases by 65% compared to the **3ReP** derivative. Similar results have been reported by Ormond and coworkers [53]. Their study showed that free-base porphyrins with *para*- and *meta*-substituted *meso*-aryl derivatives have larger ϕ_f values for all *para*-substituted cases, due to increased electron donating character at the *para*-position. Another comparison that can be made is of the porphyrin without the peripheral Re(I) complexes in the *meta* position. Unfortunately, it was not possible to measure the ϕ_f value of the *para*-substituted porphyrin without the Re(I) complexes, due to solubility and aggregation problems in most solvents. As reported by Cocca and coworkers [54], porphyrin in the absence of peripheral complexes does not significantly alter fluorescence quantum yield values, a factor attributed to the macrocycle and which may vary with the position of the pyridinic nitrogen.

Concerning the fluorescence lifetime (τ_f), it is noted that the Re(I)-porphyrins with side groups at the *para* position also exhibit similar behavior as observed for ϕ_f; τ_f is longer for porphyrins with side groups at the *para* position (Table 1). When comparing solvents, τ_f is slightly shorter in MeCN. With both ϕ_f and τ_f, the radiative rate constant (k_r) is calculated using $k_r = \Phi_f/\tau_f$ (Table 1). The low radiative rate indicates that the main relaxation processes are nonradiative, primarily through internal conversion and/or intersystem crossing rates.

To verify the contribution of both pathways, the triplet state formation quantum yield (ϕ_T) using the double fs-pulses approach, as previously described [26]. As shown in Table 1, the ϕ_T are relatively high, ranging from 37% to 48%. The relationship between ϕ_T and the *meta* and *para* side group positions is the opposite of what is observed in the ϕ_f. In the following relation, $k_{isc} = \Phi_T/\tau_f$, the intersystem crossing rate is calculated (Table 1). The results show that the intersystem crossing rates are at least one order of magnitude higher than the radiative rate. The internal conversion rate is determined using the relation $k_{ic} = 1/\tau_f - k_r - k_{isc}$ (Table 1), and as shown, these rates are also one order of magnitude higher than the k_r values. Considering the errors in the ϕ_f, ϕ_T, and τ_f, we infer that both k_{isc} and k_{ic} have comparable contributions to the nonradiative relaxation pathway for certain porphyrins. Additionally, for the **4ReP** compound in both solvents, the internal conversion is slightly higher, even when accounting for experimental errors.

3.3 | TD-DFT Theoretical Calculations

To investigate the molecular orbitals and electronic properties of **3ReP** and **4ReP**, geometry optimizations were first carried out, followed by frequency calculations. Owing to the different attachment positions of the Re(I) moiety to the *meta*- or *para*-N-pyridyl positions, the optimized geometries of **3ReP** and **4ReP** present noticeable differences (Figure S7). The main structural parameters of both complexes are summarized in the Supporting Information section (Table S2). The Re(I) moieties display very similar bond distances to the nitrogen atom of the pyridyl group (variations of 0.014 Å for **3ReP** and 0.008 Å for **4ReP**) as well as to the carbonyl ligands (variations of 0.025 Å for **3ReP** and 0.020 Å for **4ReP**). At the overall molecular level, however, more evident differences arise. Coordination of the Re(I) center to the *meta*- or *para*-N-pyridyl positions leads to a slightly more twisted porphyrin core in **3ReP** compared to **4ReP**, with a deviation of 1.55° (Figure S8). In addition, the rhenium moieties alternate between positions above and below the porphyrin plane, inducing the observed ruffled conformation of the macrocycle. Despite being relatively small, these distortions are sufficient to produce significant structural differences between the two complexes.

Structural information plays a crucial role in the analysis of electronic properties. To this end, sTDA calculations were performed employing the well-established CAM-B3LYP functional, as previously reported by Heine's group [55]. The calculated electronic

transitions are summarized in Table 2, while Figure S9 presents the overall absorption spectra of the two compounds studied in MeCN.

As observed, the calculated Soret and Q bands appear in agreement with the experimental spectra. Up to thirty electronic transitions were computed for each porphyrin derivative, resulting in a richer electronic spectrum, as expected; however, Table 2 reports only the most relevant transitions and MO plots are listed in the Supporting Information section (Figures S10 and S11). Transitions in the range of ≈250–350 nm can be mainly assigned to intraligand excitations. The Q bands are primarily attributed to highest occupied molecular orbital (HOMO)–lowest unoccupied molecular orbital (LUMO) transitions, with some contribution from LUMO + 1. In both complexes, the HOMOand LUMO exhibit similar characteristics, as reasonably expected. As illustrated in Figure 3, for **4ReP**, the HOMO is mainly localized on the nitrogen atoms of the pyrrole units and the Re(I) *d* orbitals, whereas, the LUMO is predominantly delocalized over the porphyrin macrocycle. The **3ReP** HOMO shows minimal *d* orbital contribution, which may explain the Q band delocalization between these complexes.

At first glance, the calculated band patterns might suggest a very high degree of similarity, since both compounds share a closely related composition. Nevertheless, molecular geometry introduces a decisive factor: even subtle structural differences can lead to significant variations in electronic distribution and stereochemical behavior. This structural influence helps to explain why the spectra, although broadly comparable, reveals distinct features when analyzed in detail.

Overall, the calculations carried out in this work showed good agreement with the experimental results. In particular, the comparison between calculated and experimental energy gaps proved to be satisfactory. It should be noted, however, that predicting electronic spectra solely from MO gaps can be challenging especially in such large and complex chemical systems like the ones studied here.

3.4 | CV of Porphyrins

The cyclic voltammograms of the studied porphyrins, **3ReP** and **4ReP**, in dry MeCN, are shown in Supporting Information

TABLE 2 | Soret and Q bands of 3ReP and 4ReP. Oscillator strengths are reported in parentheses, along with the corresponding wavelengths and energy gaps of the main electronic transitions.

	Soret bands			Q bands		
Porphyrin	**λ, nm**	**E_{gap}, eV**	**MO transitions**	**λ, nm**	**E_{gap}, eV**	**MO transitions**
3ReP	358.6 (0.8257)	3.258	167 → 174 (0.35)	519.6 (0.0842)	2.386	172 → 174 (0.75)
	368.1 (1.1963)	3.368	167 → 173 (0.42)	601.1 (0.0146)	2.063	172 → 173 (0.79)
4ReP	426.1 (0.9377)	2.910	169 → 175 (0.52) 168 → 174 (0.51)	534.6 (0.2167)	2.319	173 → 174 (0.79)
	428.5 (1.1628)	2.894	172 → 174 (0.67) 173 → 175 (0.39)	612.3 (0.0267)	2.025	173 → 175 (0.70)

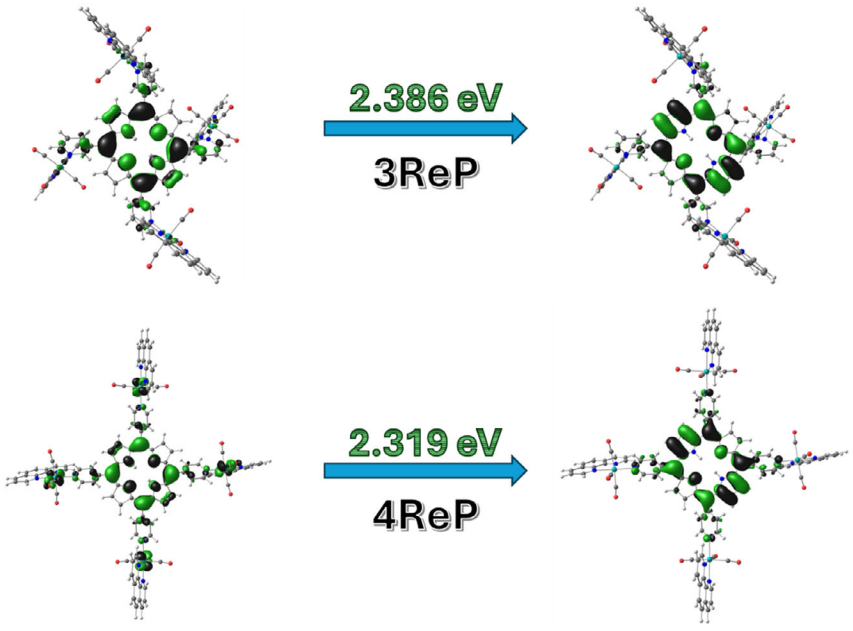

FIGURE 3 | Main frontier molecular orbitals of the porphyrins **3ReP** and **4ReP**.

section (Figure S12), and the respective redox potentials and HOMO-LUMO energies are listed in Table 3.

First, when analyzing the electrochemical behavior in the anodic region of the free-base tetra-cationic porphyrins **3ReP** and **4ReP**, two irreversible peaks are observed in the +1.50 to +2.10 V range. These can be attributed to the mono-electronic oxidations of the porphyrin ring, forming π-cation radical and di-cation species (Table 3). Moreover, during the second oxidation process, the oxidation of Re(I) ions to Re(II) can also occur simultaneously, as noted in the literature [11]. Moving to the cathodic region (from −0.50 to −1.20 V range), two irreversible peaks are observed, corresponding to the mono-electronic reduction processes of the porphyrin ring, forming π-anion radical and dianion species in solution (Table 3). Additionally, the isomeric effect (*meta* and *para* positions) does not significantly affect the redox potentials or HOMO–LUMO energies in this system.

This redox behavior can be confirmed using spectroelectrochemistry in the UV–Vis region. Generally, spectroelectrochemical studies were conducted with ≈10^{-6} M solutions of porphyrins **3ReP** and **4ReP** in MeCN for the oxidation and reduction processes. For instance, the spectroelectrochemistry results for porphyrin **3ReP** are depicted in Figure 4.

For compound **3ReP**, oxidation in the 0.0– +1.80 V range (Figure 4a) led to a decrease in absorbance in the Soret band without a blue- or red-shift, along with a slight increase in absorbance at 864 nm, likely indicating the occurrence of the first mono-electronic oxidation of the porphyrin ring, forming π-cation radical species. Finally, when the applied potential ranged from +1.80 to +2.30 V (Figure 4b), the absorbance of the Soret band decreased significantly, accompanied by an increase in the intensity of the UV band at 273 nm, Q-bands red-shift, and a decrease in the low-intensity and broad band at 864 nm. This result is attributed to the second mono-electronic oxidation of the porphyrin ring, leading to dication species formation in solution, simultaneously with the Re(I) complex oxidation.

At the negative potential range, the reduction of porphyrin **3ReP** from 0.0 to −0.70 V (Figure 4c) showed a decrease in the intensity of the Soret band, concomitant with an increase in absorbance at 452 nm and slightly increasing absorption in the Q-bands region. This can be attributed to the first mono-electronic reduction of

TABLE 3 | Redox potential data of derivatives 3ReP and 4ReP, in dry MeCN (*E* versus NHE).

Porphyrin	E_{red1}, V[a]	E_{red2}, V[a]	E_{ox1}, V[b]	E_{ox2}, V[b]	E_{HOMO}, eV[c]	E_{LUMO}, eV[d]	ΔE[e]
3ReP	−0.59	−1.13	+1.64	+2.06	−6.04	−3.81	2.23
4ReP	−0.57	−1.10	+1.64	+2.08	−6.04	−3.83	2.21

[a]E_{pc} = cathodic peak.
[b]E_{pa} = anodic peak.
[c]E_{HOMO} = −[4.4 + first E_{ox} (versus NHE)]eV.
[d]E_{LUMO} = −[4.4 + first E_{red} (versus NHE)]eV.
[e]ΔE, E_{LUMO} − E_{HOMO}.

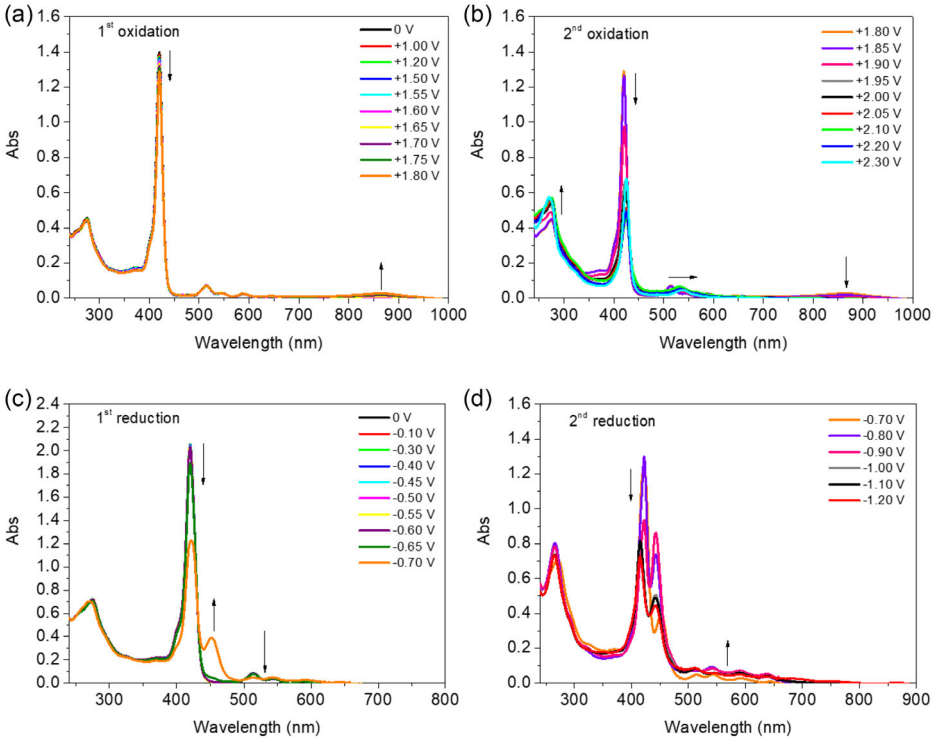

FIGURE 4 | Spectroelectrochemistry of porphyrin **3ReP** in MeCN with 0.1 M $TBAPF_6$, during oxidation: (a) from 0.0 to +1.80 V, (b) from +1.80 to +2.30 V, (c) from 0.0 to −0.70 V, and (d) from −0.70 to −1.20 V.

the porphyrin ring, forming the π-radical anion. Finally, when the potential was shifted to between −0.70 and −1.20 V (Figure 4d), the absorption spectral changes are attributed to the second mono-electronic reduction of the porphyrin ring to the dianion species, indicated by the decreased absorbance in the Soret band. Moreover, all spectroelectrochemical data for porphyrin **4ReP** are presented in Supporting Information section (Figure S13).

3.5 | Aggregation Assays, Stability in Solution, and Log P_{OW} Values

The aggregation behavior of tetra-cationic porphyrins **3ReP** and **4ReP** in solution was evaluated using UV–Vis analysis in both pure DMF and a DMF (5%)/Tris-HCl pH 7.4 buffer solution. Generally, no shift in maximum absorbance wavelength was observed. For example, porphyrin **3ReP** exhibited a linear increase in intensity in both solutions as the concentration varied from 1.0 to 25 μM in DMF and from 0.55 to 15 μM in the DMF (5%)/Tris-HCl pH 7.4 buffer solution, respectively (Figure 5). A slight tendency toward aggregation was observed in both cases. Additionally, the UV–Vis aggregation spectra of compound **4ReP** are available in Supporting Information section (Figure S14). Regarding stability, both derivatives remained stable in solution for up to 7 days, with data provided in Supporting Information section (Figures S15). Lastly, the log P_{OW} values of the tetra-cationic porphyrin derivatives **3ReP** and **4ReP** vary according to the position of the peripheral N-pyridyl group in the porphyrin structure. The results are listed in Supporting Information s ection (Table S3). Notably, the *meta*-isomer exhibits a lower log P_{OW} value than the corresponding *para*-isomer, likely due to the higher dipole moment induced by the out-of-plane arrangement of positively charged peripheral Re(I)-phen complexes, as documented in the literature [26, 38].

3.6 | Photobiological Properties

3.6.1 | ROS Detection by EPR

The EPR experiments commenced by measuring the kinetics of $^1O_2$ generation from the studied porphyrins under white light conditions at an irradiance of 12 mW cm^{-2}. Singlet oxygen is a reactive species formed through nonradiative energy transfer between a photosensitizer in its excited state and molecular oxygen in its ground state ($^3O_2$). This species predominates during the irradiation assays of the analyzed photosensitizers. Singlet oxygen generation was quantified using Hydroxy-TEMP at a concentration of 100 mM in MeCN. This concentration of the hydroxy-TEMP redox probe was selected to minimize the potential degradation impact of the nitroxyl radical formed after interaction with $^1O_2$ [56].

The concentration of radicals generated under white light conditions was determined through double integration of the EPR signal (Figure 6) and compared with the signal intensity of a sample of known concentration (TEMPOL; 1.0 mM). This double integration procedure of the EPR signal was also conducted for the remaining spin traps. Upon analyzing the kinetics of $^1O_2$ generation under white light, we observed that after 14 min of photoreaction, a saturation regime in nitroxyl radical generation begins. Two hypotheses were proposed to elucidate this behavior. The first hypothesis suggests saturation of $^1O_2$ generation, potentially due to a decrease in the amount of dissolved molecular oxygen or porphyrins' photodegradation, or a critical increase in the population of porphyrins in their excited state.

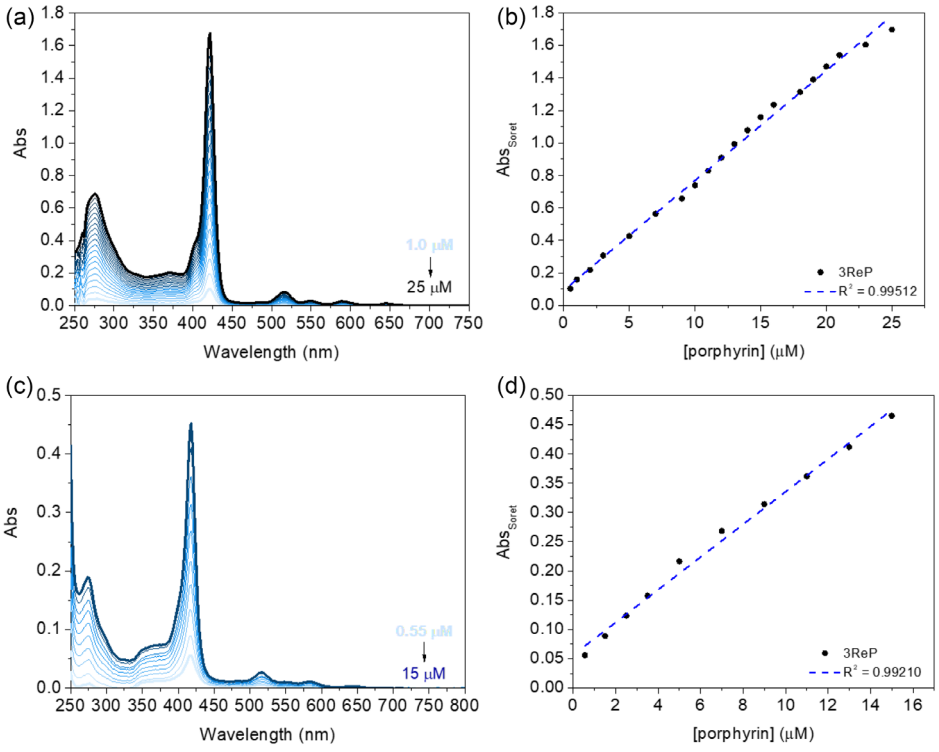

FIGURE 5 | Aggregation study for porphyrin **3ReP**, using (a) DMF or (c) DMF(5%)/Tris-HCl pH 7.4 buffer solution. The graphs in (b) and (d) demonstrate the linear behavior of the Soret band absorbance as a function of concentration.

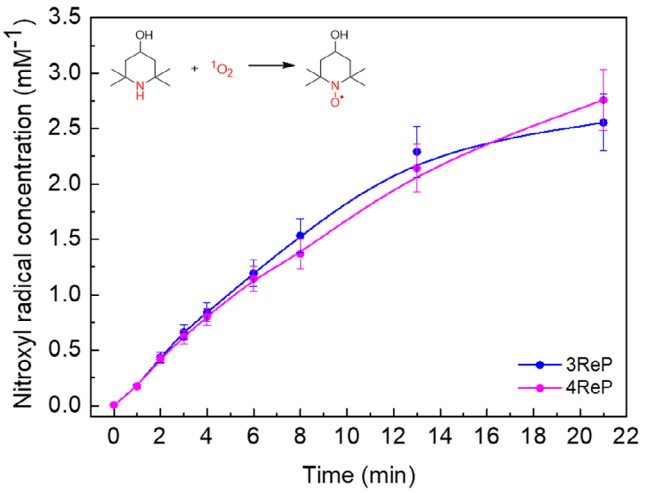

FIGURE 6 | The concentration of nitroxyl radicals formed by the interaction between singlet oxygen ($^1O_2$) and the Hydroxy-TEMP redox probe (100 mM) is shown as a function of irradiation time with a white light source (irradiance of 12 mW cm^{-2}) on the porphyrins **3ReP** and **4ReP** dissolved in MeCN.

The second hypothesis, which we consider most probable, associates with a limitation in $^1O_2$ detection by the redox probe. The upper detection limit for redox probes is between 2.0 and 10 mM of nitroxyl radicals, starting from an initial concentration of 100 mM. We exclude the involvement of nitroxyl radical degradation in the saturation of radical generation kinetics, as the detected amount of nitroxyl radical is at least an order of magnitude greater compared to systems where radical degradation occurs [50].

Regarding the efficiency of $^1O_2$ generation by porphyrin photosensitizers, the kinetics presented in Figure 5 demonstrate that both Re(I)-porphyrins perform similarly. These data will support the corroboration of $^1O_2$ measurements via DPBF photooxidation and the quantum yield values of $^1O_2$ generation.

To identify the formation of ROS other than $^1O_2$ during the illumination of the porphyrins, a PBN spin trap was used in a 200 mM acetonitrile solution, using porphyrin **3ReP** as an example. During illumination, a six-line EPR signal (Figure 7a) becomes noticeable. This signal is characteristic of the interaction of an unpaired electron (S = ½), centered on the oxygen atom, interacting with the nuclear spin from the nitrogen isotope ^{14}N (I = 1) and further split by interaction with the nuclear spin of the hydrogen isotope ^1H (I = ½) at the β position of the PBN molecule. Using Matlab and specifically the Easyspin subroutine, the spin Hamiltonian parameters of the spin adduct were obtained. These parameters allow for the identification of the reactive species trapped by the PBN. The isotropic hyperfine interaction values found were $a_N = 1.36(1)$ mT and $a_{H(\beta)} = 0.20(1)$ mT. This adduct corresponds to the capture of the OCN^- ion by the PBN molecule [57]. It is suggested that the formation of the OCN^- ion results from the oxidation of the solvent used. However, the mechanism of this oxidation process is omitted, and we do not initially identify the specific ROS involved in this process. Figure 6b illustrates the temporal evolution of the spin adduct signal intensity observed during illumination under white light conditions, as produced during PBN capture. From the results presented in Figure 7b, and by comparing them with those in Figure 6, it is evident that the concentration of ROS involved in the oxidation of acetonitrile is substantially lower compared to $^1O_2$ formation. This is an expected behavior for porphyrin-type photosensitizers, in which the dominant ROS formation mechanism is type II, involving energy transfer to molecular oxygen. Analyzing the ROS generation kinetics, we can conclude that all compounds demonstrated similar efficiencies.

To identify a potential source in the oxidation of acetonitrile, we repeated the experiments using a different solvent to solubilize PBN. We selected ethanol as the solvent to prepare aliquots of the spin traps, which were then added to the porphyrins suspended in acetonitrile, resulting in a 1:1 EtOH/MeCN ratio. In this new system, we again observed a six-line EPR signal (Figure 8), characteristic of the interaction of an unpaired electron (S = ½) centered on the oxygen atom. This unpaired electron interacts with the nuclear spin originating from ^{14}N (I = 1) and is split by the interaction with the nuclear spin of the ^1H (I = ½) at the β position of the PBN molecule.

As before, the spin Hamiltonian parameters of the spin adduct were derived by fitting the EPR spectra. For the mixed EtOH/

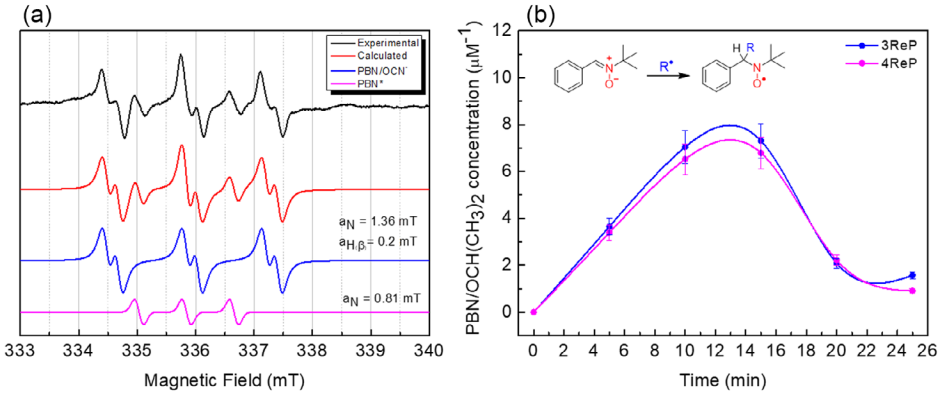

FIGURE 7 | (a) Experimental EPR spectrum (black line) and calculated spectra for the PBN spin adduct, which is characteristic of capturing the OCN^- anion (blue line), and the degradation adducts of PBN* (magenta line). These are presented alongside the calculated spectrum (red line) following exposure to white light conditions, with an irradiance of 12 mW cm^{-2}, for porphyrin **3ReP** in MeCN. (b) The concentration of spin adducts formed by the capture of the OCN^- anion by the PBN spin trap is plotted as a function of time under white light conditions for the **3ReP** and **4ReP** porphyrins in MeCN.

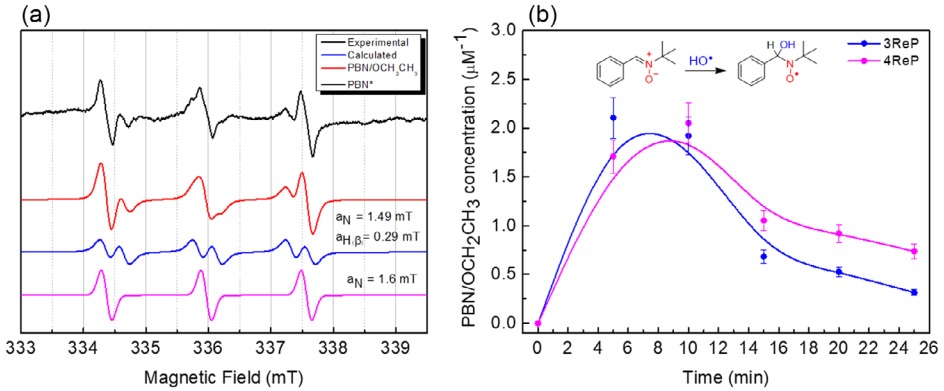

FIGURE 8 | (a) Experimental EPR spectrum (black line) and calculated spectra of the PBN spin adduct, characteristic of ethoxy radical trapping (blue line), and the PBN* degradation adduct (magenta line), together with the calculated spectrum (red line) after exposure to white light conditions (irradiance of 12 mW cm^{-2}). This setup was used for porphyrin **3ReP** dissolved in an ethanol/acetonitrile mixture (1:1). (b) Depicts the concentration of spin adducts formed by ethoxy radical trapping by the PBN spin trap as a function of irradiation time (white light - irradiance of 12 mW cm^{-2}) for porphyrin **3ReP** and **4ReP**, both dissolved in an ethanol/acetonitrile mixture (1:1).

MeCN (1:1) solvent mixture, the six-line spectra are described by hyperfine interaction values: $a_N = 1.49$ mT and $a_{H(\beta)} = 0.29$ mT (Figure 8a). This adduct corresponds to the capture of the ethoxy radical (•OCH_2CH_3) by the PBN molecule [58]; it is formed through the interaction of the hydroxyl radical (•OH) with the ethanol molecule (Figure 8a). Therefore, we have an initial indication that the ROS are formed via charge exchange between the photosensitizer and molecular oxygen. It is noteworthy that in both systems, with and without ethanol, the kinetic reaction times are similar. Additionally, the presence of a triplet EPR spectrum is noted, which is associated with the degradation of the PBN molecule itself, forming a radical detectable via EPR.

The DMPO spin trap was also used and dissolved in MeCN (300 mM). During white light irradiation, the EPR spectra of the studied porphyrins exhibited a similar line shape, as exemplified by the compound **3ReP** (Figure 9). This was characterized by the superposition of two spin adducts: (i) $DMPO/O_2^{\bullet-}$ and (ii) DMPO*. This spin adducts were identified via simulation using Easyspin software. The $DMPO/O_2^{\bullet-}$ spin adduct (red line) is characterized by the interaction of an S = ½ electron spin with a ^{14}N nucleus ($a_N = 1.30$ mT) and two additional ^1H hydrogen nuclei in distinct positions of the DMPO molecule ($a_{H(\beta)} = 1.05$ mT and $a_{H(\gamma)} = 0.29$ mT) [59]. Finally, the DMPO* spin adduct is typical for the interaction of DMPO with $^1O_2$ species and is characterized by the hyperfine interaction constant $a_N = 1.38$ mT between an electronic spin S = ½ and the nuclear spin of ^{14}N [60].

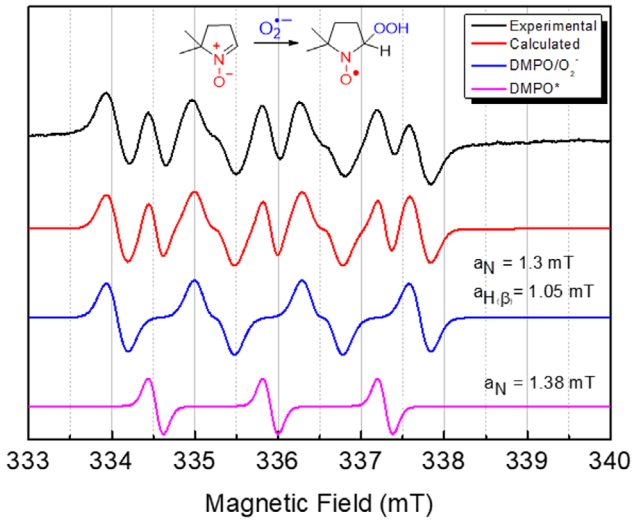

FIGURE 9 | Experimental EPR spectrum (black line) was obtained under white light irradiation conditions (irradiance of 12 mW cm^{-2}) of porphyrin **3ReP**, in conjunction with the DMPO spin trap. The simulated spectra of the $DMPO/O_2^{\bullet-}$ (blue line) and DMPO* (magenta line) spin adducts collectively form the simulated EPR spectrum (red line) that is common to both porphyrins after light exposure.

3.6.2 | Singlet Oxygen Quantum Yield and Superoxide Formation Assays

The ability of each Re(I)-porphyrin derivative to produce $^1O_2$ was studied using 1,3-DPBF photo-oxidation assays in MeCN and DMF solutions, analyzed via UV–Vis spectroscopy. Table 4 shows the DPBF photo-oxidation constants (k_{po}) and $^1O_2$ quantum yield (Φ_Δ) parameters for the studied porphyrins **3ReP** and **4ReP**. The photo-oxidation profile was monitored in the λ = 410–414 nm range by observing the decrease in DPBF absorbance during irradiation with a white light LED source (irradiance of 25 mW cm^{-2} and a total light dosage of 30 J cm^{-2}) for 10 min. All DPBF photo-oxidation spectra are provided in Supporting Information section (Figures S16–S19).

The k_{po} and Φ_Δ values for both porphyrins were quite similar, though significantly lower than the standard samples used in this work, **TPP** ($\Phi_\Delta^{std} = 0.52$ in DMSO) [34]. As observed in EPR analysis, it can be confirmed that the investigated porphyrins with peripheral Re(I) complexes exhibit a poor to moderate ability to generate $^1O_2$ in MeCN or DMF solutions.

The capacity of the studied porphyrins **3ReP** and **4ReP** to generate superoxide species ($O_2^{\bullet-}$) via a type I pathway was investigated in DMF solution. For this study, solutions of derivatives containing NBT and the reducing agent NADH were irradiated with a white light system (irradiance of 25 mW cm^{-2} and a total light dosage of 30 J cm^{-2}) under aerobic conditions for 10 min. The reaction of NBT with $O_2^{\bullet-}$ species produced diformazan, which can be monitored by the absorption band of this product centered near 530 nm. Compiled NBT reduction assays are presented in Supporting Information section (Figure S20).

TABLE 4 | Parameters of ROS generation for the studied porphyrins 3ReP and 4ReP.

Porphyrin	k_{po}, min^{-1}[a]	Φ_Δ, %[a]	k_{po}, min^{-1}[b]	Φ_Δ, %[b]	k_{SO}, min^{-1}[c]
3ReP	1.76×10^{-3}	11.0	1.40×10^{-3}	10.5	5.30×10^{-3}
4ReP	2.16×10^{-3}	13.0	0.75×10^{-3}	6.0	5.20×10^{-3}
TPP[*]	3.90×10^{-3}	52.0	3.90×10^{-3}	52.0	—

[*]TPP in DMSO as the standard molecule used in this study.
[a]In MeCN solution.
[b]In DMF solution.
[c]In DMF solution.

The superoxide generation (k_{SO}) constant for both porphyrins, as determined by the NBT reduction, is shown in Table 4, along with that of the **TPP** standard porphyrin. These results indicate that tetra-cationic porphyrins with Re(I) peripheral complexes, upon white light irradiation, can form $O_2^{\bullet-}$ in the presence of an electron donor agent (NADH), with similar values regardless of the porphyrin positional isomer (*meta* or *para*). The kinetic constant is much faster than that of the standard **TPP** sample.

Analyzing the ROS data obtained for the studied rhenium(I) derivatives, a difference can be noted between the species generated. In the case of $^1O_2$ generation (confirmed by EPR and the DFBF assay), a low generation is observed compared to the standard porphyrin **TPP**. This fact must be attributed to a disadvantage in the energy transfer process of O_2 with the peripheral Re(I) compounds, suggesting that the ROS generation mechanism may be more geared toward a process involving the redox pathway (electron transfer processes), favoring the generation of radical species. We can also note that the position of the pyridine nitrogen atom in porphyrin macrocycle, forming the *meta* and *para* position isomers, has some influence on the $^1O_2$ generation, with the **3ReP** derivative being better than the **4ReP** derivative. This may be attributed to the stereochemistry of the compound, greater solubility in the *meta* position, and a lower tendency to form aggregates in the excited state.

These highlighted facts, combined with the very closed observed values of superoxide generation (see Table 4), lead us to believe that these tetra-cationic porphyrins containing peripheral Re(I) complexes may favor the formation of radical species via a Type I mechanism.

3.6.3 | Photostability Behavior

In terms of photostability, certain dyes must remain stable when exposed to light for extended periods. Therefore, the analysis of photobleaching is a crucial parameter in studying the photodegradation process following exposure to a light source, during which ROS interact with the photosensitizer, potentially leading to degradation. Based on the changes observed in the bar graphs in Figure 9a over time, it was confirmed that Re(I)-porphyrins exhibit good stability and moderate photobleaching quantum yield (Φ_{PB}) values when irradiated with a white light LED array system for 20 min, particularly in a DMF solution. This finding can explain the relatively lower to modest ROS generation by porphyrin derivatives in all solutions, according to EPR, DPBF, and NBT analyses (Figure 10).

3.6.4 | Investigation of the Biomolecule-Porphyrin Interactions

3.6.4.1 | BSA-Binding Properties by Fluorescence Emission Assays. Using BSA as a model, we monitored the fluorescence emission between BSA protein and Re(I)-porphyrins by gradually increasing the concentrations of the porphyrin derivatives **3ReP** and **4ReP** (0–20 μM) in a DMF(5%)/Tris-HCl pH 7.4 buffer solution. Figure 11 presents a representative example using porphyrin **4ReP**. Supporting Information section (Figures S21–S28) presents all BSA-binding graph plots.

Typically, protein-molecule binding parameters can be determined using steady-state fluorescence techniques through the quenching method of amino acid residues, such as tyrosine

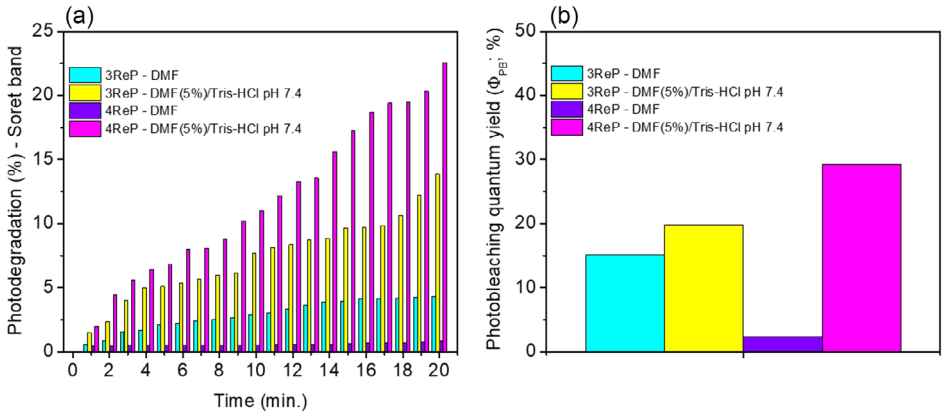

FIGURE 10 | (a) Photostability test of porphyrins **3ReP** and **4ReP** in DMF and DMF(5%)/Tris-HCl pH 7.4 buffer solution, conducted over a period of 20 min, utilizing a white light LED system with an irradiance of 25 mW cm^{-2} and a total light dosage of 60 J cm^{-2}. (b) Photobleaching quantum yield (Φ_{PB}) of porphyrins **3ReP** and **4ReP** in DMF and DMF(5%)/Tris-HCl pH 7.4 buffer solution, also measured over a period of 20 min, using a white light LED system with an irradiance of 25 mW cm^{-2} and a total light dosage of 60 J cm^{-2}.

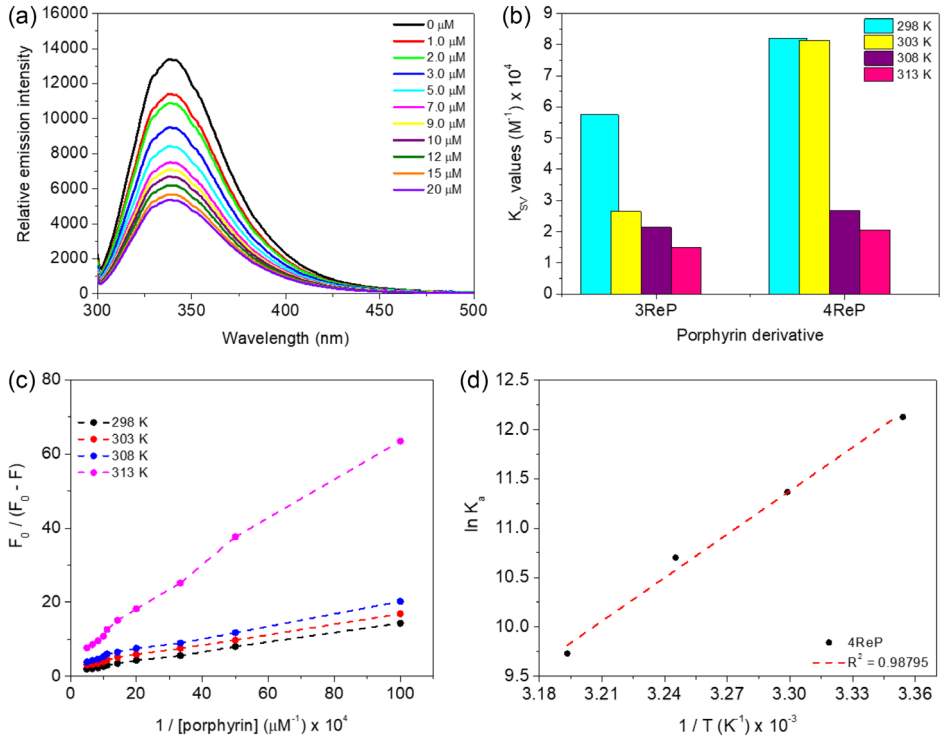

FIGURE 11 | (a) Steady-state fluorescence emission spectra for the interaction between BSA (5.0 μM) and **4ReP** porphyrin (0–20 μM) at 298 K in a buffer solution of DMF(5%)/Tris-HCl pH 7.4 buffer mixture. (b) K_{SV} values between BSA and the porphyrins **3ReP** and **4ReP** at four different temperatures. (c) Modified Stern–Volmer plots depicting the interaction between BSA and the compound **4ReP** at four different temperatures. (d) The van't Hoff plot of porphyrin **4ReP** derived from the K_a values across four different temperatures.

and tryptophan. Consequently, the interaction between BSA and each Re(I)-porphyrin derivative was assessed via the fluorescence quenching of these amino acid residues, notwithstanding substantial but unknown contributions from tyrosine residue. Figure 11a illustrates the steady-state fluorescence emission of BSA (fixed concentration at 5.0 μM) both in the absence and presence of successive additions of **4ReP** (0–20 μM) at 298 K. The fluorescence intensities of BSA at $\lambda = 339$ nm decreased progressively as the **4ReP** concentrations increased, without blue or red shifts, indicating that quenching of the Trp^{214} residue enhances its relative contribution to the emission. A similar trend was noted for the derivative **3ReP**.

It is well-established that two different mechanisms typically govern the interaction between a fluorophore and a quencher derivative: dynamic and/or static processes. These interactions may involve collisional quenching in dynamic mechanisms and nonfluorescent ground–state complex formation in static mechanisms. Notably, dynamic and static quenching can be readily distinguished by variations in temperature and through lifetime assays.

Table 5 presents the K_{SV} and k_q values for the interaction between BSA and Re(I)-porphyrin derivatives at four different temperatures (298–313 K). In all instances, K_{SV} values decreased with rising temperatures (Figure 11b). Additionally, the bimolecular quenching rate constant k_q values were approximately three orders of magnitude larger (10^{12} M^{-1} s^{-1}) than the diffusional collision quenching constant ($k_{diff} \approx 7.40 \times 10^9$ M^{-1} s^{-1}), as reported in the literature [61], suggesting that the primary fluorescence quenching mechanism is possibly via a static process. A similar behavior is observed between tetra-cationic porphyrins with peripheral Ru(II)-polypyridyl complexes and human serum albumin protein [62].

The modified Stern–Volmer plots across all temperatures for the BSA:**4ReP** interaction are shown in Figure 11c. The K_a values for each Re(I)-porphyrin derivative are on the order of 10^4 M^{-1}, indicating a moderate interaction ability with BSA (Table 5). The N-pyridyl position orientation of the Re(I) complex in the porphyrin affects the K_a value, which decreases with increasing temperature (Table 5). Thus, the modified Stern–Volmer analysis suggests that both porphyrin derivatives can be efficiently transported and biodistributed by the serum albumin model.

The forces of interaction between compounds and biomacromolecules may involve electrostatic, hydrogen bonds, van der Waals, and hydrophobic interactions, which can be evaluated using the signs and magnitudes of thermodynamic parameters, including changes in enthalpy ($\Delta H°$) and entropy ($\Delta S°$) [63]. Figure 10d depicts the van't Hoff plot for the interaction between BSA and **4ReP**. The thermodynamic parameters for each porphyrin are provided in Table 5. The negative values for $\Delta G°$ affirm the hypothesis that the binding process is spontaneous. The negative $\Delta H°$ and positive $\Delta S°$ values suggest that the binding is both enthalpically and entropically driven [64]. According to Ross and Subramanian [62], $\Delta H° < 0$ and $\Delta S° > 0$, it is plausible that electrostatic interactions significantly contribute to the binding process, which is supported by the chemical structure of **3ReP** and **4ReP**, which are positively charged [65].

3.6.4.2 | Time-Resolved Fluorescence Analysis with BSA and Porphyrins. Time-resolved fluorescence decays were performed to further validate the principal fluorescence quenching

TABLE 5 | BSA-binding parameters with porphyrins 3ReP and 4ReP in DMF (5%)/Tris-HCl, pH 7.4 buffer solution.

Porphyrin	T, K	Q, %[a]	K_{SV}, M^{-1}[b] × 10^4	k_q, $M^{-1}\,s^{-1}$[c] × 10^{12}	K_a, M^{-1}[d] × 10^4	f[e]	$\Delta H°$, kJ mol^{-1}[f]	$\Delta S°$, kJ K^{-1} mol^{-1}[f]	$\Delta G°$, kJ mol^{-1}[g]
3ReP	298	50.00	5.75 ± 0.05	9.35 ± 0.06	7.70 ± 0.04	1.40	−47.20 ± 0.03	+17.70 ± 0.06	−27.90
	303	23.00	2.65 ± 0.01	4.30 ± 0.05	7.56 ± 0.05	2.00			−28.30
	308	28.50	2.14 ± 0.02	3.47 ± 0.01	5.11 ± 0.04	1.85			−27.80
	313	33.00	1.48 ± 0.04	2.40 ± 0.02	1.17 ± 0.02	2.00			−24.40
4ReP	298	60.00	8.20 ± 0.02	12.50 ± 0.03	18.50 ± 0.02	1.50	−37.00 ± 0.03	+14.70 ± 0.06	−30.00
	303	26.00	8.14 ± 0.02	13.00 ± 0.03	8.65 ± 0.02	1.60			−28.65
	308	13.00	2.67 ± 0.05	4.34 ± 0.03	6.00 ± 0.05	1.60			−28.20
	313	33.00	2.04 ± 0.05	3.31 ± 0.05	1.68 ± 0.07	1.60			−25.30

[a]Quenching (%) = $(F_0 - F)/F_0 \times 100$.
[b]Stern-Volmer quenching constant.
[c]Stern-Volmer bimolecular quenching rate constant, using BSA lifetime ($\tau_f = 6.15$ ns).
[d]Modified Stern–Volmer constant.
[e]Number of fluorophores.
[f]Determined by van´t Hoff equation.
[g]Gibbs free-energy values determined by K_a values and $R = 0.008314$ J mol^{-1} K^{-1} and $T = 298$ to 313 K.

mechanism in the interaction between BSA and Re(I)-porphyrins. The fluorescence lifetime (τ_f) in a DMF(5%)/Tris-HCl pH 7.4 buffer solution for free BSA and BSA with derivatives **3ReP** and **4ReP** showed some differences (Table 6). All lifetime plots are available in the Supporting Information section (Figure S29).

Contrary to the steady-state fluorescence quenching analysis, the time-resolved decays obtained by excitation at 295 nm indicated the potential impact of the excitation mode on the primary fluorescence quenching mechanism. In other words, the results from the steady-state analysis, which showed a predominance of static behavior (where the tryptophan residue is selectively excited), did not mirror those from the time-resolved analysis. The latter suggested a contribution from possible dynamic interactions, which could excite the tryptophan (Trp), tyrosine (Tyr), and phenylalanine (Phe) residues. Thus, the studied porphyrins interact not only in the cavity housing the tryptophan residue but also in regions rich in Tyr and/or Phe residues. These results will be complemented and better interpreted with the help of SF and molecular docking calculations.

3.6.4.3 | SF and Site Marker Analysis with BSA. To provide insight into the molecular environment near tyrosine (Tyr) and tryptophan (Trp) amino acid residues with and without the presence of porphyrins **3ReP** and **4ReP**, SF spectra were recorded at 298 K. For Tyr residues, $\Delta\lambda = 15$ nm, and for Trp residues, $\Delta\lambda = 60$ nm. All emission spectra are detailed in the Supporting Information section (Figures S30 and S31).

In SF emission analysis, the sensitivity associated with fluorescence is maintained, offering several advantages: spectral simplification, bandwidth reduction, and avoidance of various perturbing effects [66]. In both cases, the presence of Re(I)-porphyrins decreased fluorescence intensity without shifting the maximum fluorescence emission, indicating that compounds **3ReP** and **4ReP** bind to BSA without affecting the microenvironment around the Tyr or Trp residues. Notably, the Trp residue analysis ($\Delta\lambda = 60$ nm) showed a greater decrease in intensity than the Tyr residue analysis ($\Delta\lambda = 15$ nm), suggesting that the primary interaction might occur via the tryptophan residue. These results corroborate those described in the earlier spectroscopic analysis.

Regarding the binding sites and cavities, the structure of BSA is quite similar to that of human serum albumin, possessing two primary binding pockets in hydrophobic regions: site I (the warfarin-binding site located in subdomain IIA) and site II (the ibuprofen-binding site located in subdomain IIIA). A third binding site, site III (the digitoxin-binding site in subdomain IB), was reported later. Based on molecular docking calculations, competitive binding experiments with digitoxin (site marker III) were conducted, with results presented in the Supporting Information section (Figure S32). The competitive binding experiments involved adding Re(I)-porphyrins **3ReP** and **4ReP** to a BSA:digitoxin mixture at a 1:1 concentration ratio at 298 K. As seen in the Supporting Information section (Table S4), the K_a values varied for the BSA:**3ReP** and BSA:**4ReP** interactions in the presence of digitoxin, suggesting that digitoxin (site III) affects the binding of the studied porphyrins. This behavior is consistent with previous reports on other tetra-cationic porphyrin derivatives with peripheral complexes [67].

TABLE 6 | Time-resolved parameters between BSA and the studied porphyrins (BSA = 5.0 μM and porphyrins = 20 μM).

	τ_1, ns	Relative %	τ_2, ns	Relative %	χ^2
BSA	1.87 ± 0.05	32.58	6.15 ± 0.05	67.42	1.026
BSA:3ReP	2.14 ± 0.05	32.49	5.52 ± 0.05	67.51	1.043
BSA:4ReP	1.58 ± 0.05	31.90	5.13 ± 0.05	68.10	1.099

3.6.5 | Molecular Docking Results

3.6.5.1 | In Silico Calculations for the Interaction between BSA and Porphyrins. In silico calculations using a molecular docking approach were conducted to better understand the binding capacity of BSA:3ReP and BSA:4ReP within the three main subdomains of albumin (subdomains IIA, IIIA, and IB, corresponding to sites I, II, and III). Although subdomain IIA (site I) was not suggested as a feasible binding region, subdomains IIIA and IB were identified as possible binding regions, with docking scores of 69.1 and 10.1, respectively, for BSA:3ReP and BSA:4ReP inside site II, and 75.8 and 39.9 for BSA:3ReP and BSA:4ReP inside site III. Since the highest docking scores were obtained for subdomain IB, this external region was suggested as the main binding site for 3ReP and 4ReP, agreeing with the experimental drug-displacement assays with digitoxin described above and summarized in the Supporting Information section (Figure S28 and Table S4).

This external pocket had been previously identified as a feasible site for other porphyrins, such as *meso*-tetra(thienyl)porphyrins containing peripheral Pt(II)- and Pd(II)-complexes [41], tetracationic(4-pyridyl)porphyrin both with and without peripheral Pt(II)-bipyridyl complexes [61], and *meso*-tetra(4-pyridylvinylphenyl) porphyrins coordinated to Ru(II)-polypyridyl derivatives [68] due to their large steric volume.

Figure 12 illustrates the best docking poses for BSA:3ReP and BSA:4ReP. In this scenario, both porphyrins may interact superficially in the two feasible binding sites (subdomains IIIA and IB), especially on the positive electrostatic potential surface of albumin, likely due to the aromatic core in the porphyrin structure (Figures 12a,b). Within the main binding site (subdomain IB), the porphyrins under study do not completely overlap (Figure 12c), highlighting the isomeric effects of 3ReP and 4ReP on binding, previously identified by differences in experimental binding constants. In other words, 3ReP possesses more connecting points than 4ReP (Figures 12d,e), being primarily stabilized by hydrophobic and hydrogen bond interactions (Table S5). Interestingly, in silico calculations indicated that into subdomain IB, the positively charged pyridinium moiety of the 3ReP structure might interact with negatively charged amino acid residues Glu-17 and Glu-284, while the same moiety from the 4ReP structure might interact with the negatively charged amino acid residue Glu-130, supporting the experimental detection of the contribution of electrostatic forces in the binding BSA:3ReP and BSA:4ReP.

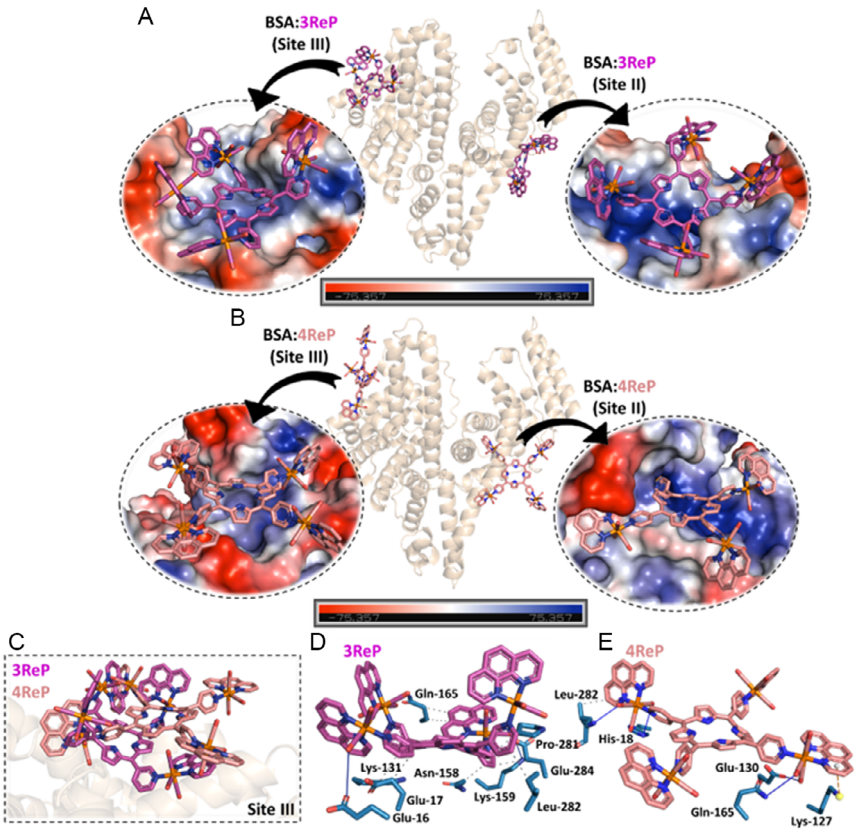

FIGURE 12 | (a) The best docking pose for the interaction BSA:**3ReP** in the two feasible binding sites, accompanied by the corresponding electrostatic potential map. (b) The best docking pose for the interaction BSA:**4ReP** in the two feasible binding sites, with the corresponding electrostatic potential map. (c) Superposition of the best docking poses for interactions between BSA and both **3ReP** and **4ReP** within subdomain IB (site III). The main amino acid residues interacting with (d) **3ReP** and (e) **4ReP** in subdomain IB (site III). The amino acid residues, **3ReP**, and **4ReP** are shown in stick representation in light blue, pink, and beige, respectively. Element colors: oxygen is red, nitrogen is dark blue, and rhenium is orange. For clarity, hydrogen atoms were omitted. Black and orange dots represent hydrophobic and π-cation interactions, respectively, while blue lines indicate hydrogen bonds.

4 | Conclusions

In summary, the results indicated that tetra-cationic porphyrins 3ReP and 4ReP are interesting scaffolds for the photosensitizer design, presenting relevant properties for future application in photodynamic processes. The insertion of the peripheral-coordinated Re(I)-carbonyl complexes resulted in increased of triplet quantum yields, weak tendency of aggregation, and good photostability, these characteristics can be useful for several applications such as solar energy conversion into chemicals, such as CO_2 photoreduction, or to sensitize other chemical reactions, including those of biological interest. About the photobiological parameters, there is a capacity of these porphyrins to generate ROS upon white light irradiation conditions, mainly radical species.

In the BSA binding study, these tetra-cationic derivatives with Re(I) complexes interact moderately and spontaneously with the albumin model, mainly by electrostatic forces, with a probable static mechanism. Future studies of these derivatives can be carried out in areas of photobiology involving applications in cancer therapy, microbiology, and photoinduced processes.

Acknowledgments

The authors would like to thank the Coordination for the Improvement of Higher Education Personnel – CAPES (Finance code 001), the National Council for Scientific and Technological Development – CNPq, the Rio Grande do Sul State Research Support Foundation – FAPERGS, and the São Paulo State Research Support Foundation – FAPESP. The Coimbra Chemistry Centre is supported by funding from the Fundação para a Ciência e a Tecnologia (FCT, the Portuguese agency for scientific research) through the projects UIDB/00313/2025 and UIDP/00313/2025. B.A.I. acknowledges the financial support provided by CNPq (PQ grants no. 303287/2024−1) and FAPERGS (PqG no. 24/2551-0001561−2 and FAPERGS/FAPESP no. 24/2551-0001939−1) and extended a special thanks to Dr. Thiago Barcellos of Universidade de Caxias do Sul for the HRMS mass analysis. A.S.P. acknowledges the financial support provided by FAPESP (grant no. 2022/07268−8) and CNPq (grant no. 305631/2022−5). L.D.B. acknowledges the financial support provided by FAPESP (grants no. 2020/16036−8, 2022/02439−9 and 2025/01908−3). K.K. acknowledges the financial support provided by CNPq (PQ no. 313155/2023−2). L.A.S.C. acknowledges the financial support provided by CNPq (PQ grants no. 305491/2024−5). O.A.C. acknowledges Programa de Pós-Graduação em Biologia Celular e Molecular from Oswaldo Cruz Foundation (Rio de Janeiro, Brazil) and CAPES for the grant PIPD (process SCBA 88887.082745/2024−00 with subproject 31010016). The authors would also like to thank Atlas Assessoria Linguística for language editing.

The Article Processing Charge for the publication of this research was funded by the Coordenação de Aperfeiçoamento de Pessoal de Nível Superior - Brasil (CAPES) (ROR identifier: 00x0ma614).

Funding

This work was supported by the CAPES (Finance Code 001); CNPq, FAPERGS, FAPESP, FAPEMIG.

Conflicts of Interest

The authors declare no conflicts of interest.

Data Availability Statement

The data that support the findings of this study are available from the corresponding author upon reasonable request.

References

1. J. A. S. Cavaleiro, J. P. C. Tomé, and M. A. F. Faustino, *Synthesis of Glycoporphyrins in Heterocycles from Carbohydrate Precursors*, Berlin: Springer, (2007): 179.

2. K. M. Kadish, K. M. Smith, and R. Guilard, *The Porphyrin Handbook*, New York: Academic Press, (2000).

3. H. E. Toma and K. Araki, *Exploring the Supramolecular Coordination, Chemistry-Based Approach for Nanotechnology, Progress in Inorganic Chemistry*, Hoboken: John Wiley & Sons, (2009): 379.

4. M. J. F. Calvete, A. V. C. Simões, C. A. Henriques, S. M. A. Pinto, and M. M. Pereira, "Tetrapyrrolic Macrocycles: Potentialities in Medical Imaging Technologies," *Current Organic Synthesis* 11 (2014): 127.

5. A. V. Muller, M. R. Gonçalves, L. D. Ramos, A. S. Polo, and K. P. M. Frin, "The Importance of the ^{3}MLCT Excited State of Ru(II), Re(I), and Ir(III) Compounds in the Development of Photosensors, OLEDs, and CO_2 Photoreduction," *Quimica Nova* 40 (2017): 200.

6. K. P. Morelli Frin, D. C. da Rocha, J. F. Mamud, and A. S. Polo, "Photoisomerization of Di-Nuclear Rhenium(I) BPE-Based Compounds," *Photochemical & Photobiological Sciences: Official Journal of the European Photochemistry Association and the European Society for Photobiology* 17 (2018): 1443.

7. J. F. Mamud, G. Biazolla, C. S. Marques, et al., "Z to E Light-Activated Isomerization of α-Pyridyl-N-Arylnitrone Ligands Sensitized by Rhenium(I) Polypyridyl Complexes," *Inorganica Chimica Acta* 514 (2021): 120009.

8. H. Kumagai, Y. Tamaki, and O. Ishitani, "Photocatalytic Systems for CO_2 Reduction: Metal-Complex Photocatalysts and Their Hybrids with Photofunctional Solid Materials," *Accounts of Chemical Research* 55 (2022): 978–990.

9. Y. Yamazaki, K. Ohkubo, D. Saito, et al., "Kinetics and Mechanism of Intramolecular Electron Transfer in Ru(II)-Re(I) Supramolecular CO_2−Reduction Photocatalysts: Effects of Bridging Ligands," *Inorganic Chemistry* 58 (2019): 11480.

10. Y. Kuramochi, O. Ishitani, and H. Ishida, "Reaction Mechanisms of Catalytic Photochemical CO_2 Reduction Using Re(I) and Ru(II) Complexes," *Coordination Chemistry Reviews* 373 (2018): 333.

11. A. V. Müller, L. A. Faustino, K. T. de Oliveira, A. O. T. Patrocinio, and A. S. Polo, "Visible-Light-Driven Photocatalytic CO_2 Reduction by Re(I) Photocatalysts with N-Heterocyclic Substituents," *ACS Catalysis* 13 (2023): 633.

12. A. V. Müller, W. M. Wierzba, L. G. A. do Nascimento, et al., "Tuning the Photocatalytic CO_2 Reduction through Para-Substituents in Bipyridyl Rhenium Complexes," *Artificial photosynthesis* 1, no. 5 (2025): 214–225, https://doi.org/10.1021/aps.4c00026.

13. P. Cavigli, G. Balducci, E. Zangrando, et al., "Structural and Photophysical Characterization of a Tin(IV) Porphyrin-Rhenium(I) (Diimine) Conjugate," *Inorganica Chimica Acta* 439 (2016): 61.

14. M. Boccalon, E. Iengo, and P. Tecilla, "New Meso-Substituted trans-A2B2 Di(4-Pyridyl)Porphyrins as Building Blocks for Metal-Mediated Self-Assembling of 4 + 4 Re(I)-Porphyrin Metallacycles," *Organic & Biomolecular Chemistry* 11 (2013): 4056.

15. A. Gabrielsson, F. Hartl, J. R. L. Smith, and R. N. Perutz, "Photo-Induced Ligand Substitution at a Remote Site via Electron Transfer in a Porphyrin-Appended Rhenium Carbonyl Supermolecule," *Chemical Communications* (2002): 950.

16. C. D. Windle, M. V. Câmpian, A.-K. Duhme-Klair, E. A. Gibson, R. N. Perutz, and J. Schneider, "CO_2 Photoreduction with Long-Wavelength Light: Dyads and Monomers of Zinc Porphyrin and Rhenium Bipyridine," *Chemical Communications* 48 (2012): 8189.

17. C. D. Windle, M. W. George, R. N. Perutz, P. A. Summers, X. Z. Sun, and A. C. Whitwood, "Comparison of Rhenium-Porphyrin Dyads for CO_2

Photoreduction: Photocatalytic Studies and Charge Separation Dynamics Studied by Time-Resolved IR Spectroscopy," *Chemical Science* 6 (2015): 6847.

18. M. Casanova, E. Zangrando, E. Iengo, et al., "Structural and Photophysical Characterization of Multichromophoric Pyridylporphyrin-Rhenium(I) Conjugates," *Inorganic Chemistry* 47 (2008): 10407.

19. M. Ghirotti, C. Chiorboli, M. T. Indelli, et al., "Energy Transfer Pathways in Pyridylporphyrin Re(I) Adducts," *Inorganica Chimica Acta* 360 (2007): 1121.

20. G. Mion, T. Gianferrara, A. Bergamo, et al., "Phototoxic Activity and DNA Interactions of Water-Soluble Porphyrins and Their Rhenium(I) Conjugates," *ChemMedChem* 10 (2015): 1901.

21. Y. Kuramochi and A. Satake, "Metalloporphyrins: Their Multitalented Nature as Observed in Multi-Metal Complex Systems," *Dalton Transactions* 52 (2023): 5418.

22. Y. Kuramochi, R. Sato, H. Sakuma, and A. Satake, "Photocatalytic CO_2 Reduction Sensitized by a Special-Pair Mimic Porphyrin Connected with a Rhenium(I) Tricarbonyl Complex," *Chemical Science* 13 (2022): 9861.

23. Y. Kuramochi, Y. Suzuki, S. Asai, et al., "Significance of the Connecting Position Between Zn(II) Porphyrin and Re(I) Bipyridine Tricarbonyl Complex Units in Dyads for Room-Temperature Phosphorescence and Photocatalytic CO_2 Reduction: Unexpected Enhancement by Triethanolamine in Catalytic Activity," *Chemical Science* 14 (2023): 8743.

24. Y. Kuramochi and A. Satake, "Photocatalytic CO_2 Reductions Catalyzed by Meso-(1,10-Phenanthrolin-2-yl)-Porphyrins Having a Rhenium(I) Tricarbonyl Complex," *Chemistry: A European Journal* 26 (2020): 16365.

25. Y. Kuramochi, K. Tanahashi, and A. Satake, "Synthesis and Photocatalytic CO_2 Reduction of a Cyclic Zinc(II) Porphyrin Trimer with an Encapsulated Rhenium(I) Bipyridine Tricarbonyl Complex," *Chemistry: A European Journal* 30 (2024): e202303324.

26. D. C. Jornada, R. Q. Garcia, C. H. da Silveira, et al., "Investigation of the Triplet Excited State and Application of Cationic Meso-Tetra(Cisplatin)Porphyrins in Antimicrobial Photodynamic Therapy," *Photodiagnosis and Photodynamic Therapy* 35 (2021): 102459.

27. B. M. Rodrigues, H. F. V. Victoria, G. Leite, et al., "Photophysical, Photobiological, and Biomolecule-Binding Properties of New Tri-Cationic Meso-Tri(2-Thienyl)Corroles with Pt(II) and Pd(II) Polypyridyl Derivatives," *Journal of Inorganic Biochemistry* 242 (2023): 112149.

28. C. Bannwarth, E. Caldeweyher, S. Ehlert, et al., "Extended Tight-Binding Quantum Chemistry Methods," *WIRES Computational Molecular Science* 11 (2020): e1493.

29. C. Bannwarth, S. Ehlert, and S. Grimme, "GFN_{2-x}TB-An Accurate and Broadly Parametrized Self-Consistent Tight-Binding Quantum Chemical Method with Multipole Electrostatics and Density-Dependent Dispersion Contributions," *Journal of Chemical Theory and Computation* 15 (2019): 1652.

30. M. Stahn, S. Ehlert, and S. Grimme, "Extended Conductor-Like Polarizable Continuum Solvation Model (CPCM-X) for Semiempirical Methods," *The Journal of Physical Chemistry. A* 127 (2023): 7036.

31. B. de Souza, "GOAT: A Global Optimization Algorithm for Molecules and Atomic Clusters," *Angewandte Chemie International Edition* 64 (2025): e202500393.

32. T. Yanai, D. P. Tew, and N. C. Handy, "A New Hybrid Exchange-Correlation Functional Using the Coulomb-Attenuating Method (CAM-B3LYP)," *Chemical Physics Letters* 393 (2004): 51.

33. T. Risthaus, A. Hansen, and S. Grimme, "Excited States Using the Simplified Tamm-Dancoff Approach for Range-Separated Hybrid Density Functionals: Development and Application," *Physical Chemistry Chemical Physics* 16 (2014): 14408.

34. F. Weigend and R. Ahlrichs, "Balanced Basis Sets of Split Valence, Triple Zeta Valence and Quadruple Zeta Valence Quality for H to Rn: Design and Assessment of Accuracy," *Physical Chemistry Chemical Physics* 7 (2005): 3297.

35. F. Neese, "Software Update: The ORCA Program System-Version 6.0," *Computational Molecular Science* 15 (2025): e70019.

36. R. R. Gagne, C. A. Koval, and G. C. Lisensky, "Ferrocene as an Internal Standard for Electrochemical Measurements," *Inorganic Chemistry* 19 (1980): 2854.

37. F. M. Engelmann, P. Losco, H. Winnischofer, K. Araki, and H. E. Toma, "Synthesis, Electrochemistry, Spectroscopy, and Photophysical Properties of a Series of Meso-Phenylpyridylporphyrins with One to Four Pyridyl Rings Coordinated to $[Ru(bipy)_2Cl]^+$ Groups," *Journal of Porphyrins and Phthalocyanines* 6 (2002): 33.

38. F. M. Engelmann, I. Mayer, D. S. Gabrielli, et al., "Interaction of Cationic Meso-Porphyrins with Liposomes, Mitochondria, and Erythrocytes," *Journal of Bioenergetics and Biomembranes* 39 (2007): 175.

39. R. C. Pivetta, B. L. Auras, B. de Souza, et al., "Photophysical Properties and Spectroelectrochemical Characterization of 10-(4-Methyl-Bipyridyl)-5,15-(Pentafluorophenyl)Corrole," *Journal of Porphyrins and Phthalocyanines A* 332 (2017): 306.

40. V. B. de Souza, V. N. da Rocha, P. C. Piquini, O. A. Chaves, and B. A. Iglesias, "Effects of Substituents on the Photophysical/Photobiological Properties of Mono-Substituted Corroles," *Molecules* 28 (2023): 1385.

41. I. Tisoco, M. C. Donatoni, H. F. V. Victória, et al., "Photophysical, Photooxidation, and Biomolecule-Interaction of Meso-Tetra(Thienyl) Porphyrins Containing Peripheral Pt(II) and Pd(II) Complexes: Insights for Photodynamic Therapy Applications," *Dalton Transactions* 51 (2022): 1646.

42. I. Tisoco, M. H. Köhler, P. A. Nogara, et al., "Study on the Photophysical Property of Meso-Tetra(2-Fluorenyl)Porphyrin Derivatives and Their Interactions with DNA/HSA Biomacromolecules," *Inorganica Chimica Acta* 556 (2023): 121639.

43. S. C. Santamarina, D. A. Heredia, A. M. Durantini, and E. N. Durantini, "Antimicrobial Photosensitizing Material Based on Conjugated Zn(II) Porphyrins," *Antibiotics* 11 (2022): 91.

44. Y. B. Palacios, S. O. Simonetti, C. H. Chavez, et al., ""Illuminated Glycoporphyrins": A Photodynamic Approach for Candida albicans Inactivation," *Journal of Photochemistry and Photobiology. B, Biology* 264 (2025): 113105.

45. T. V. Acunha, B. M. Rodrigues, J. A. da Silva, et al., "Unveiling the Photophysical, Biomolecule Binding, and Photo-Oxidative Capacity of Novel Ru(II)-Polypyridyl Corroles: A Multipronged Approach," *Journal of Molecular Liquids* 340 (2021): 117223.

46. T. Bessega, O. A. Chaves, F. M. Martins, et al., "Coordination of Zn(II), Pd(II), and Pt(II) with Ligands Derived from Diformylpyridine and Thiosemicarbazide: Synthesis, Structural Characterization, DNA/BSA Binding Properties, and Molecular Docking Analysis," *Inorganica Chimica Acta* 496 (2019): 119049.

47. A. Bujacz, "Structures of Bovine, Equine, and Leporine Serum Albumin," *Acta Crystallographica Section D* D68 (2012): 1278.

48. F. M. Martins, D. C. Durigon, O. A. Chaves, R. A. Peralta, D. F. Back, and Hernán Terenzi, "Zwitterionic Dioxidovanadium(V) Complexes Containing Fluorinated Triphenylphosphonium Ligands: Structure and Biomacromolecule Studies," *New Journal of Chemistry* 48 (2024): 17722.

49. E. R. S. Paz, V. G. Isoppo, F. S. dos Santos, et al., "Imidazole-Based Optical Sensors as a Platform for Bisulfite Sensing and BSA/HSA Interaction Study: An Experimental and Theoretical Investigation," *Journal of Molecular Liquids* 387 (2023): 122666.

50. B. M. Rodrigues, C. C. Diniz, M. H. Köhler, O. A. Chaves, and B. A. Iglesias, "Fluorenyl-Corroles: Characterization, Photophysical,

Photobiological, and DNA/BSA-Binding Properties of Novel Examples," *Journal of Photochemistry and Photobiology A* 460 (2025): 116112.

51. O. A. Chaves, B. A. Iglesias, and C. Serpa, "Biophysical Characterization of the Interaction Between a Transport Human Plasma Protein and the 5,10,15,20-Tetra(Pyridine-4-yl)Porphyrin," *Molecules* 27 (2022): 5341.

52. C. H. da Silveira, O. A. Chaves, A. C. Marques, N. M. P. Rosa, L. A. S. Costa, and B. A. Iglesias, "Synthesis, Photophysics, Computational Approaches, and Biomolecule Interactive Studies of Metalloporphyrins Containing Pyrenyl Units: Influence of the Metal Center," *European Journal of Inorganic Chemistry* 2022, no. 12 (2022): e202200075.

53. A. B. Ormond and H. S. Freeman, "Effects of Substituents on the Photophysical Properties of Symmetrical Porphyrins," *Dyes and Pigments* 96 (2013): 440.

54. L. H. Z. Cocca, F. Gotardo, L. F. Sciuti, T. V. Acunha, B. A. Iglesias, and L. De Boni, "Investigation of Excited Singlet State Absorption and Intersystem Crossing Mechanism of Isomeric Meso-Tetra(Pyridyl) Porphyrins Containing Peripheral Polypyridyl Platinum(II) Complexes," *Chemical Physics Letters* 708 (2018): 1.

55. K. Batra, S. Zahn, and T. Heine, "Benchmark of Simplified Time-Dependent Density Functional Theory for UV-Vis Spectral Properties of Porphyrinoids," *Advanced Theory and Simulations* 3 (2019): 1900192.

56. H. F. V. Victória, D. C. Ferreira, J. B. Gabriel, et al., "Detection of Singlet Oxygen by EPR: The Instability of the Nitroxyl Radicals," *Free Radical Biology & Medicine* 180 (2022): 143.

57. L. Eberson, "'Inverted Spin Trapping': Reactions Between the Radical Cation of α-Phenyl-N-tert-Butylnitrone and Ionic and Neutral Nucleophiles," *Journal of the Chemical Society, Perkin Transactions* 2 (1992): 1807.

58. A. Ledwith, P. Russell, and L. H. Sutcliffe, "Alkoxy Radical Intermediates in the Thermal and Photochemical Oxidation of Alcohols," *Proceedings of the Royal Society A* 332 (1973): 151.

59. K. Reszka and C. F. Chignell, "Spin-Trapping of the Superoxide Radical in Aprotic Solvents," *Free Radical Research Communications* 14 (1991): 97.

60. P. Bilski, K. Reszka, M. Bilska, and C. F. Chignell, "Oxidation of the Spin Trap 5,5-Dimethyl-1-Pyrroline N-Oxide by Singlet Oxygen in Aqueous Solution," *Journal of the American Chemical Society* 118 (1996): 1330.

61. M. Montalti, A. Credi, L. Prodi, and M. T. Gandolfi, *Handbook of Photochemistry*, 3rd ed. (CRC Press, Taylor & Francis, 2006).

62. O. A. Chaves, L. B. Menezes, and B. A. Iglesias, "Multiple Spectroscopic and Theoretical Investigation of Meso-Tetra-(4-Pyridyl) Porphyrin-Ruthenium(II) Complexes in HSA-Binding Studies: Effect of Zn(II) in Protein Binding," *Journal of Molecular Liquids* 294 (2019): 111581.

63. P. D. Ross and S. Subramanian, "Thermodynamics of Protein Association Reactions: Forces Contributing to Stability," *Biochemistry* 20 (1981): 3096.

64. J. R. Lakowicz, *Principles of Fluorescence Spectroscopy* New York, NY, USA: Springer, (2006).

65. O. A. Chaves, L. S. de Barros, M. C. C. de Oliveira, et al., "Biological Interactions of Fluorinated Chalcones: Stimulation of Tyrosinase Activity and Binding to Bovine Serum Albumin," *Journal of Fluorine Chemistry* 199 (2017): 30.

66. T. V. Acunha, O. A. Chaves, B. A. Iglesias, and J. Porphyr, "Fluorescent Pyrene Moiety in Fluorinated C6F5-Corroles Increases the Interaction with HSA and CT-DNA," *Phthalocyanines* 25 (2021): 75.

67. O. A. Chaves, T. V. Acunha, B. A. Iglesias, C. S. H. Jesus, and C. Serpa, "Effect of Peripheral Platinum(II) Bipyridyl Complexes on the Interaction of Tetra-Cationic Porphyrins with Human Serum Albumin," *Journal of Molecular Liquids* 301 (2020): 112466.

68. V. Viecelli, O. A. Chaves, K. Araki, P. R. Martins, and B. A. Iglesias, "Synthesis, Characterization, Spectroelectrochemical, Photophysical, and HSA-Binding Properties of Novel and Versatile Meso-Tetra(4-Pyridylvinylphenyl)Porphyrins Coordinated to Ruthenium(II)-Polypyridyl Derivatives," *Journal of the Brazilian Chemical Society* 31 (2020): 2282.

Supporting Information

Additional supporting information can be found online in the Supporting Information section. **Supporting Fig. S1:** HRMS-ESI of porphyrin **3ReP**. **Supporting Fig. S2:** HRMS-ESI of porphyrin **4ReP**. **Supporting Fig. S3:** FTIR-ATR spectrum of porphyrin **3ReP**. **Supporting Fig. S4:** FTIR-ATR spectrum of porphyrin **4ReP**. **Supporting Fig. S5:** ^{1}H NMR spectrum of porphyrin **3ReP** in DMSO-d_6. **Supporting Fig. S6:** ^{1}H NMR spectrum of porphyrin **4ReP** in DMSO-d_6. **Supporting Fig. S7:** Optimized geometry for **3ReP** (above) and **4ReP** (below) with different views. **Supporting Fig. S8:** Opposite pyrrole rings detached by two planes which are twisted. **Supporting Fig. S9:** Superimposed calculated absorption spectra of **3ReP** (red) and **4ReP** (black). **Supporting Fig. S10:** Molecular orbital representations of porphyrin **3ReP**. **Supporting Fig. S11:** Molecular orbital representations of porphyrin **4ReP**. **Supporting Fig. S12:** Voltamogramms of studied porphyrins **3ReP** and **4ReP**, in MeCN solution, using $TBAPF_6$ 0.1 M as supporting electrolyte, at scan rate 100 mV s^{-1}. **Supporting Fig. S13:** Spectroelectrochemistry of porphyrin **4ReP** in MeCN with 0.1 M $TBAPF_6$, during oxidation: (a) from 0.0 to +1.80 V, (b) from +1.80 to +2.30 V, (c) from 0.0 to −0.90 V, and (d) from −0.90 to −1.40 V. **Supporting Fig. S14:** Aggregation study for porphyrin **4ReP**, using (a) DMF or (c) DMF (5%)/Tris-HCl pH 7.4 buffer solution. The graphs in (b) and (d) demonstrate the linear behavior of the Soret band absorbance as a function of concentration. **Supporting Fig. S15:** Solution stability study for porphyrin **3ReP** and **4ReP**, using (a) DMF or (b) DMF (5%)/Tris-HCl pH 7.4 buffer solution at period of 7 days. **Supporting Fig. S16:** DPBF photooxidation assay with porphyrin **3ReP** in MeCN, during irradiation with a white light LED source (irradiance of 25 mW cm^{-2} and a total light dosage of 30 J cm^{-2}) for 10 minutes. **Supporting Fig. S17:** DPBF photooxidation assay with porphyrin **4ReP** in MeCN, during irradiation with a white light LED source (irradiance of 25 mW cm^{-2} and a total light dosage of 30 J cm^{-2}) for 10 minutes. **Supporting Fig. S18:** DPBF photooxidation assay with porphyrin **3ReP** in DMF, during irradiation with a white light LED source (irradiance of 25 mW cm^{-2} and a total light dosage of 30 J cm^{-2}) for 10 minutes. **Supporting Fig. S19:** DPBF photooxidation assay with porphyrin **4ReP** in DMF, during irradiation with a white light LED source (irradiance of 25 mW cm^{-2} and a total light dosage of 30 J cm^{-2}) for 10 minutes. **Supporting Fig. S20:** NBT photoreduction assay with porphyrins **3ReP** and **4ReP** in DMF, during irradiation with a white light LED source (irradiance of 25 mW cm^{-2} and a total light dosage of 30 J cm^{-2}) for 10 minutes. **Supporting Fig. S21:** Steady-state fluorescence emission spectra for the interaction between BSA (5.0 μM) and **3ReP** porphyrin (0–20 μM) at 298 K in a DMF(5%)/Tris-HCl pH 7.4 buffer mixture. **Supporting Fig. S22:** Steady-state fluorescence emission spectra for the interaction between BSA (5.0 μM) and **3ReP** porphyrin (0–20 μM) at 303 K in a DMF(5%)/Tris-HCl pH 7.4 buffer mixture. **Supporting Fig. S23:** Steady-state fluorescence emission spectra for the interaction between BSA (5.0 μM) and **3ReP** porphyrin (0–20 μM) at 308 K in a DMF(5%)/Tris-HCl pH 7.4 buffer mixture. **Supporting Fig. S24:** Steady-state fluorescence emission spectra for the interaction between BSA (5.0 μM) and **3ReP** porphyrin (0–20 μM) at 313 K in a DMF(5%)/Tris-HCl pH 7.4 buffer mixture. **Supporting Fig. S25:** Steady-state fluorescence emission spectra for the interaction between BSA (5.0 μM) and **4ReP** porphyrin (0–20 μM) at 298 K in a DMF(5%)/Tris-HCl pH 7.4 buffer mixture. **Supporting Fig. S26:** Steady-state fluorescence emission spectra for the interaction between BSA (5.0 μM) and **4ReP** porphyrin (0–20 μM) at 303 K in a DMF(5%)/Tris-HCl pH 7.4 buffer mixture. **Supporting Fig. S27:** Steady-state fluorescence emission spectra for the interaction between

BSA (5.0 μM) and **4ReP** porphyrin (0–20 μM) at 308 K in a DMF(5%)/Tris-HCl pH 7.4 buffer mixture. **Supporting Fig. S28:** Steady-state fluorescence emission spectra for the interaction between BSA (5.0 μM) and **4ReP** porphyrin (0–20 μM) at 313 K in a DMF(5%)/Tris-HCl pH 7.4 buffer mixture. **Supporting Fig. S29:** Lifetimes plots for the interaction between BSA (5.0 μM) and **3ReP** and **4ReP** porphyrins (20 μM) in a DMF(5%)/Tris-HCl pH 7.4 buffer mixture, using NanoLED at 284 nm as excitation source. **Supporting Fig. S30:** SF spectra between BSA (5.0 μM) and porphyrin **3ReP** (0-20 μM) in a DMF(5%)/Tris-HCl pH 7.4 buffer mixture where (a) 15 nm and (b) 60 nm. **Supporting Fig. S31:** SF spectra between BSA (5.0 μM) and porphyrin **4ReP** (0-20 μM) in a DMF(5%)/Tris-HCl pH 7.4 buffer mixture where (a) 15 nm and (b) 60 nm. **Supporting Fig. S32:** Competitive assays by steady-state fluorescence emission spectra between BSA:digitoxin (1:1) and porphyrin (a) **3ReP** and (b) **4ReP** (0-20 μM) in a DMF(5%)/Tris-HCl pH 7.4 buffer mixture. **Supporting Table S1:** Elemental analysis and molar condutivity of derivatives. **Supporting Table S2:** Main bond distances for Re(I) centers from xTB optimized geometry of the derivatives **3ReP** and **4ReP**. **Supporting Table S3:** Log P_{OW} for porphyrin **3ReP** and **4ReP**. **Supporting Table S4:** K_a values between BSA and porphyrin **3ReP** and **4ReP**, in de absence or presence of digitoxin site marker III at 298 K. **Supporting Table S5:** Molecular docking results for the interaction BSA:**3ReP** and BSA:**4ReP** inside subdomain IB (site III).